Monthly Notices of the ROYAL ASTRONOMICAL SOCIETY

MNRAS **533,** 2893–2915 (2024) https://doi.org/10.1093/mnras/stae1955
Advance Access publication 2024 August 13

Magnetic field, magnetospheric accretion, and candidate planet of the young star GM Aurigae observed with SPIRou

B. Zaire [1,2]★ J.-F. Donati [2] S. P. Alencar,[1] J. Bouvier,[3] C. Moutou,[2] S. Bellotti,[4] A. Carmona,[3] P. Petit,[2] Á. Kóspál,[5,6] H. Shang,[7] K. Grankin,[8] C. Manara [9] E. Alecian,[3] S. P. Gregory [10] and P. Fouqué [2] the SLS consortium

[1] *Universidade Federal de Minas Gerais, Belo Horizonte, 31270-901 MG, Brazil*
[2] *IRAP, Université de Toulouse, CNRS / UMR 5277, CNES, UPS, 14 avenue E. Belin, F-31400 Toulouse, France*
[3] *Université Grenoble Alpes, CNRS, IPAG, F-38000 Grenoble, France*
[4] *Leiden Observatory, Leiden University, PO Box 9513, NL-2300 RA Leiden, the Netherlands*
[5] *Konkoly Observatory, HUN-REN Research Centre for Astronomy and Earth Sciences, Konkoly-Thege Miklós út 15-17, 1121 Budapest, Hungary*
[6] *Institute of Physics and Astronomy, ELTE Eötvös Loránd University, Pázmány Péter sétány 1/A, 1117 Budapest, Hungary*
[7] *Institute of Astronomy and Astrophysics, Academia Sinica, 10617 Taipei, Taiwan*
[8] *Crimean Astrophysical Observatory, 298409 Nauchny, Republic of Crimea*
[9] *European Southern Observatory, Karl-Schwarzschild-Straße 2, D-85748, Garching bei München, Germany*
[10] *SUPA, School of Science and Engineering, University of Dundee, Nethergate, DD1 4HN, Dundee, UK*

Accepted 2024 August 9. Received 2024 August 7; in original form 2024 June 7

ABSTRACT

This paper analyses spectropolarimetric observations of the classical T Tauri star (CTTS) GM Aurigae collected with SPIRou, the near-infrared spectropolarimeter at the Canada–France–Hawaii Telescope, as part of the SLS and SPICE Large Programs. We report for the first time results on the large-scale magnetic field at the surface of GM Aur using Zeeman Doppler imaging. Its large-scale magnetic field energy is almost entirely stored in an axisymmetric poloidal field, which places GM Aur close to other CTTSs with similar internal structures. A dipole of about 730 G dominates the large-scale field topology, while higher order harmonics account for less than 30 per cent of the total magnetic energy. Overall, we find that the main difference between our three reconstructed maps (corresponding to sequential epochs) comes from the evolving tilt of the magnetic dipole, likely generated by non-stationary dynamo processes operating in this largely convective star rotating with a period of about 6 d. Finally, we report a 5.5σ detection of a signal in the activity-filtered radial velocity data of semi-amplitude $110 \pm 20\,\mathrm{m\,s^{-1}}$ at a period of 8.745 ± 0.009 d. If attributed to a close-in planet in the inner accretion disc of GM Aur, it would imply that this planet candidate has a minimum mass of $1.10 \pm 0.30\,M_{\mathrm{Jup}}$ and orbits at a distance of 0.082 ± 0.002 au.

Key words: techniques: polarimetric – planets and satellites: detection – stars: formation – stars: magnetic field – stars: variables: T Tauri, Herbig Ae/Be – stars: individual: GM Aur.

1 INTRODUCTION

T Tauri stars (TTSs) are late-type pre-main-sequence (PMS) stars that are precursors of solar-like stars. These objects can be classified as classical T Tauri stars (CTTSs) when they show evidence of ongoing accretion from a surrounding disc and, later, as weak-line TTSs when accretion ceases due to the depletion of the inner disc. The study of TTSs has been crucial in advancing our understanding of planet formation and evolution, as their circumstellar discs are believed to be natural birthplaces for planets.

Stellar magnetic fields impact the accretion process in CTTSs through a mechanism known as magnetospheric accretion (see review by Hartmann, Herczeg & Calvet 2016). CTTSs indeed possess kG magnetic fields that can truncate the inner disc and channel material on to the stellar surface through accretion funnels (e.g. Bouvier et al. 2007; Alencar et al. 2012). The star–disc magnetospheric interactions also affect angular momentum transport through accretion, winds, and jets, thereby impacting stellar evolution (Bouvier et al. 2014). Simultaneously, TTSs undergo gravitational contraction during their PMS evolution, leading to rapid changes in their internal structure. Variations in internal structure and stellar rotation period are believed to play a critical role in the dynamo mechanism that allegedly amplifies the magnetic field in these stars (e.g. Stelzer & Neuhäuser 2001). There is direct observational evidence of the relationship of surface field strengths, age, and rotation (e.g. Vidotto et al. 2014). Various theoretical models of self-excited dynamos also demonstrate distinct magnetic field solutions when internal structure and rotation rates vary (e.g. Zaire et al. 2016; Emeriau-Viard & Brun 2017; Guerrero et al. 2019; Brun et al. 2022). These results suggest that the convection zone depth, rotation period, and radial mass distribution can impact the dynamo action. Overall, it is clear that

★ E-mail: zaire@fisica.ufmg.br

the study of TTSs can help elucidate the magnetic field amplification process as the internal structure and rotation rate rapidly change during this evolutionary phase.

Only in the past two decades have studies of TTSs made it possible to directly reconstruct large-scale magnetic fields using Zeeman-Doppler imaging (ZDI; Semel 1989; Donati & Brown 1997; Donati et al. 2006). Several optical and near-infrared spectropolarimetric programmes, such as the 'Magnetic Protostars and Planets' (MaPP), 'Magnetic Topologies of Young Stars and the Survival of massive close-in Exoplanets' (MaTYSSE), 'History of the Magnetic Sun' (HMS; Folsom et al. 2016), and more recently, the 'SPIRou Legacy Survey' (SLS; Donati et al. 2020b), conducted at the Canada–France–Hawaii Telescope (CFHT) have contributed to mapping the large-scale magnetic fields of TTSs. These studies unveiled in particular a correlation between the complexity of the magnetic field and the internal structure of the star (Gregory et al. 2012), similar to that observed on main-sequence M dwarfs (Morin et al. 2010). Stars with fully or largely convective interiors exhibit strong axisymmetric poloidal fields dominated by low-order spherical harmonics components such as the dipole and octupole. In contrast, TTSs with substantial radiative interiors display weaker and more complex fields, often featuring a significant toroidal component (Donati et al. 2013). However, the sample of CTTSs stars with reconstructed large-scale magnetic fields remains limited given the complicated effects induced by accretion process, whose temporal variability occurs on various time-scales. Only a few dozen CTTSs have been analysed to date, such as V2129 Oph (Donati et al. 2007, 2011a); BP Tau (Donati et al. 2008); CV Cha and CR Cha (Hussain et al. 2009); V2247 Oph (Donati et al. 2010a); AA Tau (Donati et al. 2010b); TW Hya (Donati et al. 2011b, 2024b); V4046 Sgr (Donati et al. 2011c); GQ Lup (Donati et al. 2012); DN Tau (Donati et al. 2013); LkCa 15 (Donati et al. 2019); CI Tau (Donati et al. 2020a); HQ Tau (Pouilly et al. 2020); V2062 Oph (Bouvier et al. 2020); V807 Tau (Pouilly et al. 2021); DQ Tau (Pouilly et al. 2023); DK Tau (Nelissen et al. 2021, 2023); and S CrA N (Nowacki et al. 2023).

In a complementary approach, researchers have also turned to global dynamo simulations to gain insights into the physical mechanisms governing the geometry of dynamo-generated magnetic fields (e.g. Christensen 2010; Gastine, Duarte & Wicht 2012; Yadav et al. 2015). These early simulations, albeit conducted with values of viscosity and turbulence that are not representative of actual stellar conditions, have managed somehow to reproduce the tentative link between interior and large-scale topology suggested by observations (Gregory et al. 2012). They have shown the interplay between magnetic complexity and Rossby number, which represents the ratio between the stellar rotation period and the typical time-scale of a convective cell, thus encompassing both the influence of rotation and internal structure. However, the generalization of these findings to more realistic stellar parameters remains a topic of ongoing discussion (e.g. Raynaud, Petitdemange & Dormy 2015; Brun et al. 2022; Zaire et al. 2022b), as it is their extension to CTTSs as accretion is not considered in any of these simulations. Increasing the sample of CTTSs with reconstructed large-scale magnetic fields is therefore essential to impose more constraints on dynamo models and deepen our understanding of the physical mechanisms that drive the generation and evolution of magnetic fields in TTSs.

In this paper, we present spectropolarimetric observations collected with SPIRou, the near-infrared (nIR) spectropolarimeter installed at CFHT (Donati et al. 2020b). With these observations, we can investigate the large-scale magnetic field and the magnetospheric accretion process of the CTTS GM Aurigae. We provide a brief overview of the evolutionary status of GM Aur in Section 2 and describe our observations in Section 3. The investigation of longitudinal magnetic fields from Zeeman signatures in circularly polarized line profiles is presented in Section 4, while in Section 5 we use ZDI to reconstruct the brightness distribution and large-scale magnetic field topology at the surface of GM Aur. In Section 6, we use the photospheric absorption lines to inspect radial velocity (RV) fluctuations induced by activity. Our results are discussed and summarized in Section 7.

2 THE STAR–DISC SYSTEM GM AURIGAE

The PMS star GM Aurigae is a young solar analogue located at a distance of $155.0^{+1.4}_{-2.0}$ pc (Gaia Collaboration et al. 2021) in the Taurus-Aurigae star formation region (Bertout & Genova 2006). The star, classified as K6 (Herczeg & Hillenbrand 2014), hosts a circumstellar disc that has been extensively studied to look for the presence of forming planets.

The spectral energy distribution (SED) of GM Aur shows excess infrared emission with a deficit in the near- to mid-infrared (Strom et al. 1989). SED modelling shows that GM Aur is surrounded by a disc with a large dust cavity (Rice et al. 2003; Calvet et al. 2005; Hornbeck et al. 2016). Spatially resolved (sub)millimetre observations confirm the existence of a transitional disc inclined at $52.77^\circ \pm 0.05^\circ$ with respect to the line of sight with an inner dusty cavity radius of 30–40 au (Macías et al. 2018; Francis & van der Marel 2020; Huang et al. 2020). Yet, a consensus has not been reached on whether the dust-depleted cavity was carved by undetected planet(s), by photoevaporation, magnetohydrodynamic (MHD) disc winds or a combination of all (see e.g. Izquierdo et al. 2023). Further, an inner disc of gas inclined by $68^{\circ+17^\circ}_{-28^\circ}$ has been detected within the dust cavity using observations from VLTI/GRAVITY (Bohn et al. 2022, but see also Salyk et al. 2009; Huang et al. 2020; Bosman et al. 2021). Although less precise than the transition disc inclination, these measurements suggest that GM Aur's inner and outer discs can be considered aligned as argued by Bohn et al. (2022). Furthermore, the inner disc presumably feeds the accretion process resulting in accretion rates ranging from 0.2×10^{-8} to 2.15×10^{-8} $M_\odot\,yr^{-1}$ (Ingleby et al. 2013, 2015; Manara et al. 2014; Robinson & Espaillat 2019; Bouvier et al. 2023; Wendeborn et al. 2024a).

Long-term photometry of GM Aur has shown low-level variability due to surface spots, and indicates a stellar rotation period in the range of 5.8–6.1 d (Percy et al. 2010; Robinson, Espaillat & Rodriguez 2022). More recently, Bouvier et al. (2023) analysed LCOGT light curves of GM Aur that overlap with part of the observations studied in this paper. The authors found modulations consistent with a period of 6.04 ± 0.15 d. Likewise, they used spectroscopy to demonstrate that the inverse P Cygni profiles of near-infrared accretion lines (He I 1083 nm, Pa β, Br γ), whose subcontinuum absorption traces accretion funnels rotating into and out of view (e.g. Hartmann, Hewett & Calvet 1994; Muzerolle, Calvet & Hartmann 2001; Edwards et al. 2006), are consistent with the 6.04 d period obtained from photometry.

By combining the line-of-sight-projected equatorial rotation velocity inferred from our spectropolarimetric analysis ($v_{\rm eq}\,\sin i = 13.5 \pm 0.2\,{\rm km\,s^{-1}}$, Section 5.2), rotation period ($P_{\rm rot} = 6.04 \pm 0.15$ d, equation 1), effective temperature ($T_{\rm eff} = 4287 \pm 35$ K estimated with spectral synthesis, Bouvier et al. 2023), and assuming that the rotation axis of the star coincides with that of the disc ($i = 52.77^\circ \pm 0.05^\circ$), we get a stellar radius of $R_\star = 2.02 \pm 0.06\,R_\odot$. With this radius estimate, we infer a bolometric luminosity equal to $1.25 \pm 0.08\,L_\odot$. These radius and luminosity estimates are both

Table 1. Properties of GM Aur.

Parameter	Value	Comments	Reference
Distance (pc)	$155.0^{+1.4}_{-2.0}$		1
Age (Myr)	~ 1.5	From HR diagram	Section 2
Spectral type	K6		2,3
$M_\star$ ($M_\odot$)	0.95 ± 0.05	From HR diagram	Section 2
$T_{\rm eff}$ (K)	4287 ± 35		4
i (°)	52.77 ± 0.05	From outer disc	5
$\upsilon_{\rm eq}\ \sin i$ (km s^{-1})	13.5 ± 0.2	From ZDI optimization	Section 5
$P_{\rm rot}$ (d)	6.04	Used to phase data	4
$P_{\rm rot}$ (d)	$6.03^{+0.03}_{-0.04}$	From B_ℓ data	Section 4
$P_{\rm rot}$ (d)	5.99 ± 0.01	From RV data	Section 6
$R_\star \sin i$ ($R_\odot$)	1.61 ± 0.05	From $\upsilon_{\rm eq}\ \sin i$ and $P_{\rm rot}$	Section 2
$R_\star$ ($R_\odot$)	2.02 ± 0.06	From $\upsilon_{\rm eq}\ \sin i$, $P_{\rm rot}$ and i	Section 2
$\upsilon_{\rm rad}$ (km s^{-1})	14.9 ± 0.3		Section 6
$L_\star$ ($L_\odot$)	1.25 ± 0.08	From $T_{\rm eff}$ and $R_\star$	Section 2
log g (dex)	3.80 ± 0.03	From $M_\star$ and $R_\star$	
ξ (km s^{-1})	1.7		6
$r_{\rm cor}$ ($R_\star$)	6.8 ± 0.2		Section 7
$r_{\rm m}$ ($R_\star$)	4.1 ± 1.0		Section 7

Note. (1) Gaia Collaboration (2021); (2) Herczeg & Hillenbrand (2014); (3) Luhman (2018); (4) Bouvier et al. (2023); (5) Macías et al. (2018); (6) D'Orazi, Biazzo & Randich (2011).

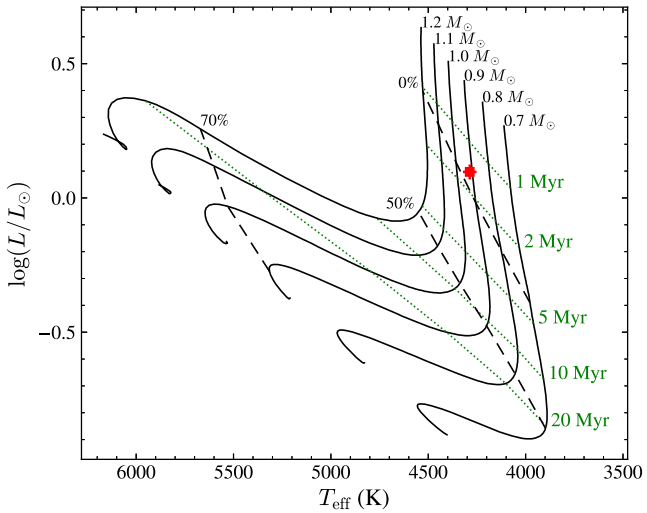

Figure 1. Location of GM Aur (red square) in the HR diagram constructed from Baraffe et al. (2015) evolutionary models. Pre-main sequence evolutionary tracks are for stellar masses of 0.7, 0.8, 0.9, 1.0, 1.1, and 1.2 $M_\odot$ (black solid lines). Isochrones are for ages of 1, 2, 5, 10, and 20 Myr (dotted green lines). Dashed black lines mark the internal structure change, corresponding to the location where the radiative core starts forming and when its radius reaches 50 per cent and 70 per cent of the stellar radius.

higher than those obtained previously by Bouvier et al. (2023), derived from the median J magnitude ($J = 9.42$), and respectively equal to $1.7 \pm 0.2\,R_\odot$ and $0.9 \pm 0.2\,L_\odot$. The difference can presumably be attributed to cool spots at the surface reducing the luminosity (Gully-Santiago et al. 2017). Table 1 summarizes the stellar properties of GM Aur used in our paper.

Fig. 1 illustrates the evolutionary stage of GM Aur. Its location in the Hertzsprung–Russell (HR) diagram, compared to the PMS stellar evolutionary tracks of Baraffe et al. (2015), indicates an age of ~ 1.5 Myr and a stellar mass of $0.95 \pm 0.05\,M_\odot$. This mass range is consistent, within a 3σ level, with the independent measurement made by Simon et al. (2017), who analysed CO emission lines from GM Aur's circumstellar disc to infer a dynamical mass of $1.14 \pm 0.02\,M_\odot$. Regarding its internal structure, GM Aur lies near the fully convective limit. Evolutionary models suggest the star is fully convective for a luminosity of $1.25 \pm 0.08\,L_\odot$ (red square in Fig. 1), while for a luminosity of $0.9 \pm 0.2\,L_\odot$ it may possess a small radiative core, estimated to be up to $0.2 \pm 0.1\,R_\star$ and comprising no more than 15 per cent of the stellar mass.

In the following, we consider that GM Aur is a star of mass $0.95\,M_\odot$ and of radius $2.02 \pm 0.06\,R_\odot$. We adopt the ephemeris of Bouvier et al. (2023) to compute the rotation cycle E:

$$\mathrm{BJD} = 2459460.80 + 6.04E. \quad (1)$$

It is worth noting that the period determination of Bouvier et al. (2023) is based on LCOGT light curves that were collected simultaneously with the first two SPIRou runs analysed in this paper. Therefore, using the same ephemeris eases the comparison between both studies.

3 SPECTROPOLARIMETRIC OBSERVATIONS

Spectropolarimetric observations of GM Aur were collected from September 2021 to January 2023 using SPIRou at CFHT. These observations were part of the CFHT Large Programs called 'SPIRou Legacy Survey'[1] (SLS; PI: Jean-François Donati) and SPICE (PI: Jean-François Donati). Studying the impact of magnetic fields on star/planet formation is one of the main science goals of SLS and SPICE.

SPIRou operates in the nIR domain, covering wavelengths from 950 to 2500 nm at a resolving power $\mathcal{R} \sim 70\,000$ (Donati et al. 2020b). Raw frames were processed with the SPIRou reduction pipeline APERO (Cook et al. 2022), which produces wavelength calibrated continuum normalized spectra corrected of telluric absorption. Data products are thus used to extract unpolarized (Stokes I) and polarized (Stokes V) spectra by the SPIROU-POLARIMETRY[2] package. The package follows the prescription of Donati et al. (1997) for optimal extraction of the polarized spectra. It combines four consecutive subexposures obtained in different orientations of the polarimeter quarter-wave Fresnel rhombs, chosen to minimize spurious polarization signatures (Cook et al. 2022). For GM Aur, 49 polarized spectra were derived from the sequences of 4 subexposures (each lasting 552 s). The journal of observations is summarized in Table A1.

3.1 Least squares deconvolution

Least-squares deconvolution (LSD; Donati et al. 1997) is applied to all observations to generate average Zeeman signatures with an enhanced signal-to-noise ratio. LSD Stokes I and V profiles are generated with the open-source software LSDPY[3], which uses a list of photospheric absorption lines and user-defined normalization parameters to determine average pseudo-profiles. We use the VALD3 data base[4] (Piskunov et al. 1995) to build an atomic absorption line mask for GM Aur that covers the spectral domain of SPIRou. A MARCS model atmosphere (Gustafsson et al. 2008) with an effective temperature of 4250 K, a logarithmic surface gravity of 4.0, and

[1] http://spirou.irap.omp.eu/Observations/The-SPIRou-Legacy-Survey
[2] https://github.com/edermartioli/spirou-polarimetry
[3] `LSDpy` is available at https://github.com/folsomcp/LSDpy.
[4] VALD3 is publicly available at http://vald.astro.uu.se.

microturbulence $\xi = 1.7\,\mathrm{km\,s^{-1}}$ is considered, all of which agree with the stellar parameters of GM Aur (see Table 1). In particular, the logarithmic surface gravity considered roughly agrees with estimates based on the stellar mass and radius ($\log g = 3.80 \pm 0.03$) and previously reported in the literature ($\log g = 3.91^{0.06}_{-0.08}$; Flores et al. 2022). As an additional condition, we remove from the line mask those lines whose absorption depth is lower than 5 per cent of the continuum (before any kind of broadening). Altogether, our line mask contains a total of 2476 spectral features. Normalization parameters needed to compute LSD profiles are the central wavelength λ_0, the line depth d, and the effective Landé factor $g_{\rm eff}$. Based on the median values of our line mask, we set $\lambda_0 = 1700$ nm, $d = 0.19$, and $g_{\rm eff} = 1.25$. Stokes V LSD profiles show average noise levels with respect to the unpolarized continuum of 1.22×10^{-4} to 2.04×10^{-4} (median of 1.49×10^{-4}). The null polarization check N (as defined in Donati et al. 1997) is consistent with 0 at all times (see Appendix B), confirming that the polarimeter performs as expected.

We also considered an alternative molecular line mask based on the magnetic-insensitive transitions from the CO molecule. The mask includes the CO bandhead lines in the wavelength range from 2200 to 2400 nm, displaying a mean wavelength of 2354 nm. The LSD profiles obtained from the CO bandhead lines are considered only in Section 6. Hereafter, unless we explicitly mentioned otherwise, whenever Stokes I and V LSD profiles are mentioned they refer to profiles from atomic lines.

We double-checked that both our polarized spectra and LSD profiles yielded similar results to those independently obtained with the alternate reduction package LIBRE-ESPRIT and LSD code outlined in Donati et al. (2023b).

3.2 Correcting for the veiling

Photospheric lines of CTTSs are veiled by excess continuum emission (Hartigan, Edwards & Ghandour 1995; Hartmann et al. 2016) that has different origins depending on the spectral domain. While accretion shocks are often the main source of optical veiling, the warm inner disc is thought to emit most of the radiation that veils the nIR spectral domain (e.g. Johns-Krull & Valenti 2001). For GM Aur, Sousa et al. (2023) found a veiling wavelength dependence in which the Y-band veiling was consistent with 0, while in the J, H, and K bands it was 0.13, 0.11, 0.31, respectively. Moreover, Bouvier et al. (2023) showed that the veiling contribution in the JHK bands varies over time in a periodic way, featuring a maximum value around the rotational phase 0. As our paper aims to investigate line profile variations caused by features at the stellar photosphere, we must first remove the veiling variability introduced on Stokes I and V LSD profiles.

Fluctuations in the equivalent width (EW) of Stokes I LSD profiles are primarily affected by veiling but can also probe temperature variations at the surface of the star (e.g. LkCa 4; Gully-Santiago et al. 2017; Finociety et al. 2023a). Assuming that the effect of veiling largely dominates, one can mitigate it by scaling Stokes I and V LSD profiles to ensure a constant EW in the data set. To suppress the veiling variability, we scale the LSD profiles to ensure a constant EW of $1.11\,\mathrm{km\,s^{-1}}$ in the data set. The results of the EW measurements before applying the scaling procedure are presented in Table A1. Equivalent widths ranged from 0.84 to $1.11\,\mathrm{km\,s^{-1}}$ (Table A1), with a median value of $1.02\,\mathrm{km\,s^{-1}}$. See Appendix B for further discussion about the calculus of unveiled Stokes I and V LSD profiles.

4 LONGITUDINAL MAGNETIC FIELD

We used the SPECPOLFLOW package[5] to estimate the longitudinal magnetic field (B_ℓ in Gauss) as the first-order moment of Stokes V LSD profiles (Donati et al. 1997):

$$B_\ell = -2.14 \times 10^{11} \frac{\int \upsilon \cdot V(\upsilon) \mathrm{d}\upsilon}{\lambda_0 \cdot g_{\rm eff} \cdot c \cdot \int [1 - I(\upsilon)] \mathrm{d}\upsilon}, \quad (2)$$

where c is the speed of the light in $\mathrm{km\,s^{-1}}$, υ is the Doppler velocity in the stellar rest frame (also in $\mathrm{km\,s^{-1}}$), and λ_0 (in nm) and $g_{\rm eff}$ are the wavelength and magnetic sensitivity of the average LSD profile, i.e. the normalization quantities used to compute Stokes I and V LSD profiles (Section 3.1). We adopted the $\upsilon_{\rm rad}$ estimation of $14.94\,\mathrm{km\,s^{-1}}$ (see Section 6) to place Stokes I and V LSD profiles in the stellar rest frame. Table A1 presents B_ℓ measurements obtained after evaluating the integral of equation (2) in a velocity window of $\pm 35\,\mathrm{km\,s^{-1}}$. The values of B_ℓ ranged from -158 to -30 G, with a median value of -107 G and a standard deviation of 32 G.

We modeled the longitudinal magnetic field evolution using Gaussian Process (GP) regression. We selected for the GP model a quasi-periodic kernel added of a white noise kernel, whose ability to recover stellar rotation periods has been demonstrated in previous studies (Donati et al. 2017; Yu et al. 2017; Angus et al. 2018; Petit et al. 2021), and that is defined as

$$K(t, t') = \eta_1^2 \exp\left[-\frac{(t-t')^2}{2\eta_3^2} - \frac{1}{2\eta_4^2}\sin^2\left(\frac{\pi(t-t')}{\eta_2}\right)\right] + \eta_5^2 \delta(t - t'). \quad (3)$$

Five GP hyperparameters control the kernel. The hyperparameter η_1 describes the semi-amplitude of the GP, η_2 the rotation period of the star, η_3 the decay time (likely the typical time-scale of evolution of active regions), η_4 the level of harmonic complexity allowed in the fit (the smaller, the more complex the fit), and η_5 the white noise (in case formal error bars are underestimated, e.g. as a result of intrinsic variability). To obtain the best statistical GP model of B_ℓ and its associated uncertainties, we maximized the log of the marginal likelihood function $\mathcal{L}_M$:

$$2 \log \mathcal{L}_M = -n \log(2\pi) - \boldsymbol{y}^T (\boldsymbol{K} + \boldsymbol{\Sigma})^{-1} \boldsymbol{y} - \log |\boldsymbol{K} + \Sigma|, \quad (4)$$

where n is the number of measurements, $\boldsymbol{y}$ is the B_ℓ data, $\boldsymbol{K}$ is the GP kernel covariance matrix, and Σ is a diagonal matrix of the data variance.

We conducted a Markov Chain Monte Carlo (MCMC) exploration over the GP hyperparameter space using the EMCEE package (Foreman-Mackey et al. 2013)[6] to sample the posterior distribution. We adopted uniform prior probability distributions for the hyperparameters η_1, η_3, η_4, and η_5 (Table 2). In contrast, we assumed a Gaussian prior for η_2, centred on 6.04 d (Bouvier et al. 2023). We initialized the MCMC sampler with 32 walkers. Chains ran until a convergence criterion of 230 times the autocorrelation time τ[7] was reached. The first $50\,\tau$ were discarded as burn-in. MCMC chains featured an autocorrelation time τ equal to 525 steps.

Fig. 2 shows the posterior distributions obtained from the MCMC exploration. We quote in Table 2 the median values of the posterior

[5]The SPECPOLFLOW package is publicly available at https://github.com/folsomcp/specpolFlow.

[6]The EMCEEPYTHON package is freely available at https://github.com/dfm/emcee.

[7]Autocorrelation times are defined as the number of iterations necessary for the MCMC sample to become independent of previous draws for each GP hyperparameter (Goodman & Weare 2010). In this study, we define as τ the largest value among the autocorrelation times estimated for a chain.

Table 2. GP parameters obtained when fitting a quasi-periodic kernel to individual time series longitudinal field data of GM Aur. The first and second columns indicate the hyperparameter and its associated variable name used throughout the paper. The third column shows the best value obtained in the GP fit, whereas the last column indicates the prior distribution adopted – for which $\mathcal{N}$ stands for Gaussian distribution and $\mathcal{U}$ for uniform distribution.

Parameters	Name	Value	Prior
GP semiamplitude (G)	η_1	36^{+14}_{-8}	$\mathcal{U}(0, 1000)$
Rotation period (d)	η_2	$6.03^{+0.03}_{-0.04}$	$\mathcal{N}(6.04, 1)$
Decay timescale (d)	η_3	97^{+69}_{-38}	$\mathcal{U}(0, 1000)$
Smoothing factor	η_4	$0.33^{+0.14}_{-0.13}$	$\mathcal{U}(0.1, 3)$
White noise (G)	η_5	0 ± 6	$\mathcal{U}(-1000, 1000)$

distributions, taken as representative of the best-fitting solution. Fig. 3 illustrates the best-fitting GP model of B_ℓ, which fits the data down to a reduced-χ^2 of 0.7 and displays a root-mean-square (RMS) value of 11 G in the residuals. The rotation period of $6.03^{+0.03}_{-0.04}$ d obtained from the analysis of B_ℓ agrees within uncertainties with the estimation in our companion study by Bouvier et al. (2023), who investigated the variability in the light curve of GM Aur and found a periodicity of 6.04 ± 0.15 d.

5 ZEEMAN-DOPPLER IMAGING

In this section, we use the tomographic method used in a series of works (Brown et al. 1991; Donati & Brown 1997; Donati et al. 2006) to reconstruct the large-scale magnetic field morphology of GM Aur using time-series Stokes I (unpolarized) and V (polarized) LSD profiles.

5.1 ZDI process

ZDI is an inversion method that maps brightness and magnetic inhomogeneities in the stellar photosphere from phase-resolved sets of Stokes I and V LSD profiles. The basic assumption behind ZDI is that these distortions/signatures mainly vary in time as a result of rotational modulation. To achieve this, ZDI divides the surface of the star into a grid of N cells (here, set to 4000 cells). These cells are independent of each other for brightness imaging. In contrast, magnetic images are described as a spherical-harmonics (SH) expansion (as described in Donati et al. 2006 and using the coefficient modification detailed in Lehmann & Donati 2022). The optimization procedure is initialized from a featureless brightness and magnetic image. Then, ZDI uses Maximum Entropy principles to iteratively search for images that maximize the entropy, defined as the amount of information in the image, whilst aiming for a data fit at a given value of reduced-χ^2 (see Skilling & Bryan 1984, for a description of the maximum entropy regularization procedure). Like in previous studies of TTSs (Donati et al. 2008), we employ a weighting scheme in the image entropy calculation that favours even SH modes when reconstructing magnetic maps.

To compute the χ^2 statistics, ZDI calculates the disc-integrated Stokes I and V profiles using modelled magnetic field and brightness images obtained at each iteration.[8] Following the definition of Morin et al. (2008), we write the synthetic Stokes profiles in terms of the filling factors f_I and f_V:

$$I = f_I \cdot I_M + (1 - f_I) \cdot I_Q, \tag{5}$$

and

$$V = f_V \cdot V_M, \tag{6}$$

where f_I represents the typical fractional area of a cell that is filled with small-scale magnetic fields and f_V accounts for the typical fractional area filled with large-scale magnetic fields capable of producing net circularly polarized signatures (see Kochukhov 2021, for visual examples of the impact of filling factors on the surface magnetic field). Under this formulation, I_Q represents the local absorption line profile obtained from non-magnetic regions, whereas I_M and V_M correspond to local Stokes I and V profiles from magnetic regions. I_M and V_M are computed using Unno-Rachkovsky's solution to the radiative transfer equation (Landi Degl'Innocenti & Landolfi 2004, Chapter 9.8).

The model parameters adopted for GM Aur follow previous nIR studies (e.g. Donati et al. 2024a). We set the filling factors to $f_I = 0.8$ and $f_V = 0.4$, meaning that 20 per cent of the stellar surface is non-magnetic. Those filling factors are similar to what was suggested by Zeeman broadening studies of the CTTS CI Tau (Sokal et al. 2020) or the young M dwarfs AD Leo (Bellotti et al. 2023) and AU Mic (Donati et al. 2023a). For the synthetic line model, we use the central wavelength of 1700 nm, Landé factor of 1.25, and Doppler width of 3.5 km s^{-1} (similar to Donati et al. 2023a; Finociety et al. 2023b). Moreover, we truncate the SH expansion of the magnetic field components at modes $\ell = 10$. Given GM Aur's value of $\upsilon_{\rm eq} \sin i$, SH coefficients with $\ell > 10$ should not carry relevant information when modelling the stellar surface (e.g. Morin et al. 2008; Fares et al. 2012; Folsom et al. 2016). Finally, we assume $i = 53^\circ$ in accordance with literature values (Table 1).

One caveat of our ZDI model is that it does not handle intrinsic variability beyond differential rotation in its current version (e.g. Donati et al. 2017; Finociety et al. 2021; Zaire, Donati & Klein 2022a) as it assumes static brightness and magnetic field maps throughout the observed window (see a recent attempt to go beyond these limitations and recover the temporal evolution of large-scale magnetic field maps in Finociety & Donati 2022). Considering the rapid evolution of GM Aur's magnetic field within a short timescale (approximately 97 d, as discussed in Section 4), we separated the SPIRou spectropolarimetric observations, spanning over 485 d, into three distinct data sets for independent analysis. These data sets comprise observations: #1 from September and 2021 October, #2 from 2021 November to 2022 January, and #3 from 2022 December to 2023 January.

5.2 ZDI surface maps of GM Aurigae

We first attempted to model brightness maps simultaneously with magnetic fields. The reconstructed ZDI images revealed only low-level brightness inhomogeneities (compared to the unspotted photosphere) that have a small impact on the Stokes I LSD profiles, suggesting that the profile broadening is mostly of magnetic origin. Given that, we chose to fit the LSD Stokes I and V profiles of GM Aur using a simple ZDI model that imposes a constant (featureless) brightness map and only takes magnetic fields into account. By exploring the principles of maximum entropy, we find that $\upsilon_{\rm eq} \sin i = 13.5 \pm 0.2$ km s^{-1} provides the best fit for the three data sets. This value is similar to previous infrared estimates of 13.7 ± 1.7 km s^{-1} using IGRINS spectra (Nofi et al. 2021).

The ZDI maximum entropy fit to the Stokes I and V LSD profiles achieved for the data sets #1, #2, and #3 are displayed in Fig. 4.

[8] Note that an alternative is to impose the brightness image in the modelling process (see Section 5.2).

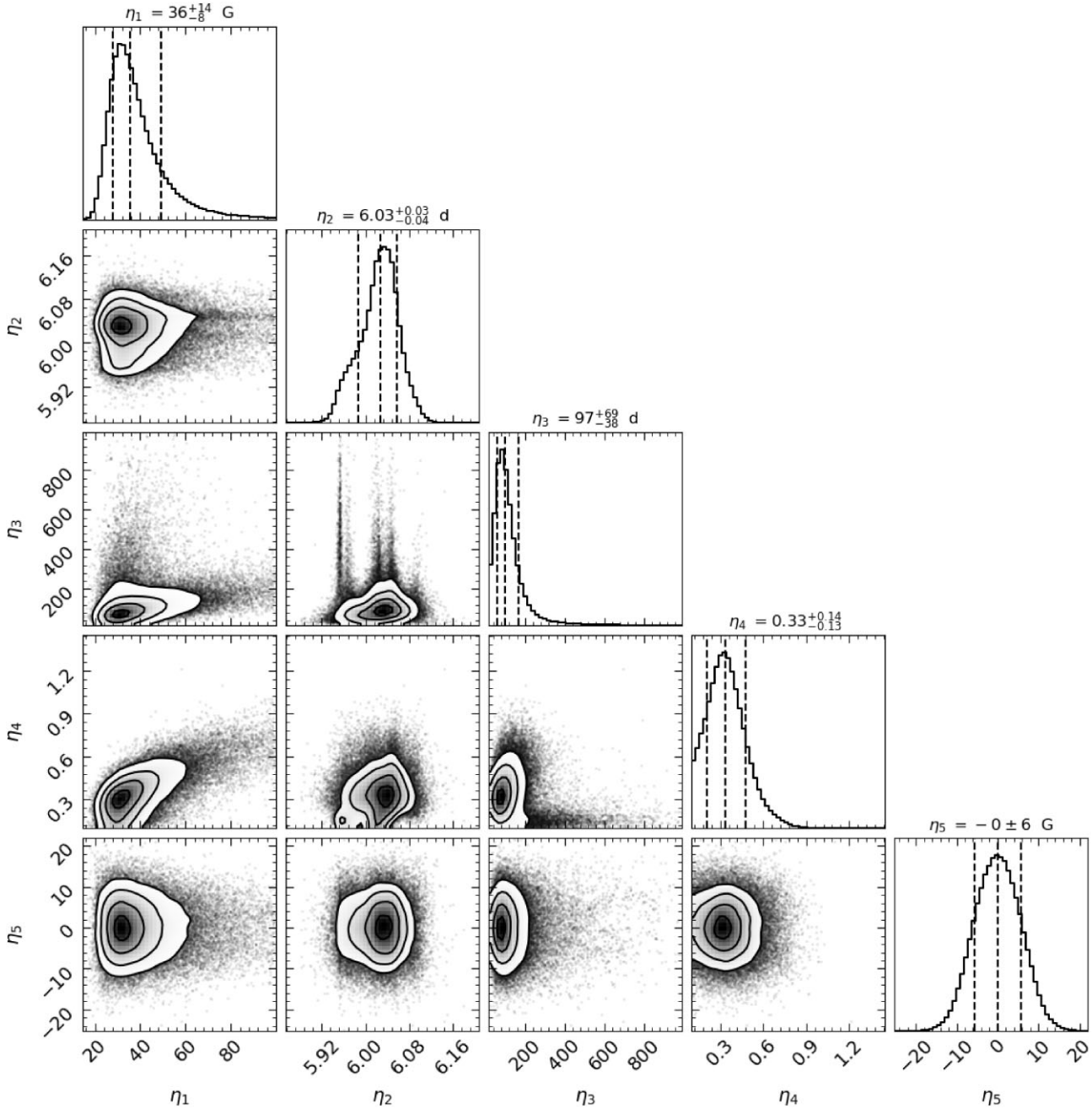

Figure 2. Posterior distributions obtained from an MCMC exploration over the hyperparameter space of the GP model of the longitudinal magnetic field evolution. The semi-amplitude η_1 and white noise η_5 are given in G, whereas the rotation period η_2 and cycle length η_3 are expressed in days, and the smoothing parameter η_4 is dimensionless. Vertical dashed lines in the histograms correspond to the 16th, 50th, and 84th percentiles of each distribution.

To obtain these ZDI models, we had to increase the error bars of the Zeeman signatures by a factor of 1.3 in order to account for intrinsic variability. This procedure allowed us to fit Stokes I and V LSD profiles down to a reduced χ^2 equal to 1 (the same factor was applied to all three data sets).

Fig. 5 presents the surface maps reconstructed for GM Aur. From left to right, columns display the surface distribution of the radial, azimuthal, and meridional magnetic field components. Overall, the large-scale magnetic topology is quite similar in all epochs. It consists of a dominant axisymmetric poloidal field that adds up to about 98 per cent of the total energy. Most of the differences between the maps are due to a minor change in the dipole field strength and orientation. The dipole that is tilted by 15° towards rotation phase 0.91 in the first epoch slightly changes its obliquity to 10° in the last two epochs, facing the rotation phase 0.95 in the second epoch and then phase 0.81 in the last epoch. In all three epochs, the negative pole of the dipolar field component is in the Northern hemisphere. As evidenced by the radial magnetic field maps, the octupolar field has the opposite polarity of the dipole field at the polar cap, resulting in nearly zero magnetic field strengths at colatitudes lower than 30°.

While it is notoriously difficult to estimate the errors in maps reconstructed with ZDI, previous studies applied a bootstrap technique

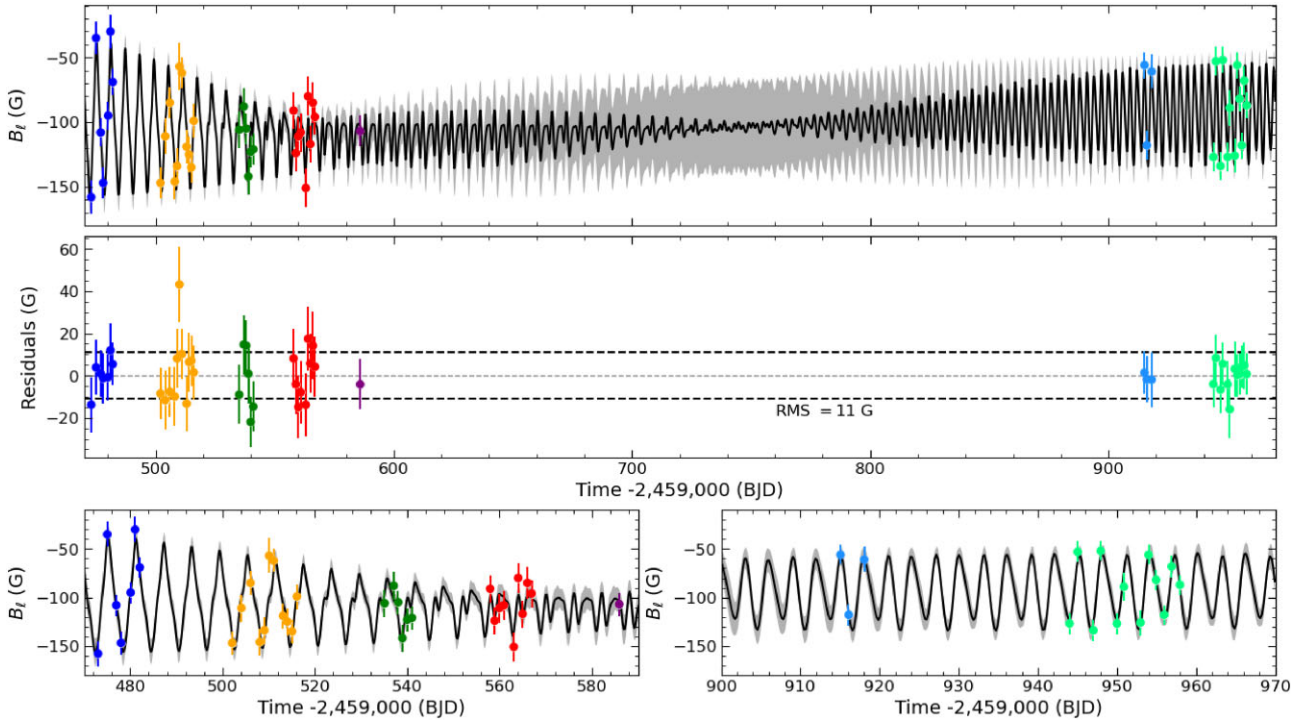

Figure 3. Gaussian process analysis of the longitudinal magnetic field of GM Aur. The top panel illustrates longitudinal magnetic field measurements (coloured circles) alongside the GP-prediction values (black line). 1σ error bars are depicted for both measurements and predictions. Colours represent SPIRou runs: September (blue), October (orange), November (green), and December 2021 (red), January and December 2022 (purple and light blue, respectively), and January 2023 (light green). The second panel shows residuals (observed minus modeled field). The last row offers detailed views of observations from October 2021 to January 2022 (left-hand panel) and December 2022 to January 2023 (right-hand panel).

to test the robustness of the magnetic images (e.g. Zaire, Donati & Klein 2021, 2022a; Strassmeier, Carroll & Ilyin 2023). These works suggest error bars typically equal to 5 per cent for field strengths, and up to 10° on the field inclinations. Assuming similar uncertainties, these results indicate that the minor changes in our magnetic maps are real and mostly reflect a dipolar field excursion.

For completeness, we summarized in Table 3 the main properties of the magnetic field geometries derived in this study. We provide the maximum magnetic field strength at the stellar surface ($B_{\rm max}$), and the fractional energy stored in the poloidal ($E_{\rm Pol}$) and toroidal ($E_{\rm Tor}$) field components. In addition, we report the distribution of poloidal field energy into dipolar ($E_{\rm Dip}$), quadrupolar ($E_{\rm Quad}$), and octupolar ($E_{\rm Oct}$) components. The fraction of poloidal energy on axisymmetric modes and the level of axisymmetry of the dipole field ($E_{\rm Dip}$) are also displayed in Table 3, along with the tilted dipole field strength ($B_{\rm Dip}$) and obliquity β.

6 RADIAL VELOCITY

We estimated RV variations of GM Aur by computing a Gaussian fit to the Stokes *I* LSD profiles from atomic lines and those from CO bandhead lines (see Table A1). Our measurements using LSD profiles from atomic lines show a mean value $\upsilon_{\rm rad} \equiv \langle RV \rangle$ of 14.94 km s^{-1} and a standard deviation of 0.31 km s^{-1}, which is consistent with earlier spectroscopic estimations of 14.95 ± 0.98 km s^{-1} (McGinnis, Bouvier & Gallet 2020). In contrast, the RVs obtained from CO lines are shifted by 0.63 km s^{-1} with respect to the atomic lines. They feature a mean value of 15.57 km s^{-1} and a standard deviation of 0.27 km s^{-1}. We observe a statistically significant positive correlation, represented by a Pearson correlation coefficient of 0.87, between the RVs obtained from atomic lines and CO lines.

Similar to the procedure described in Section 4, we jointly model the RV curves from atomic lines and CO lines using GP regression. The GP models from atomic and CO lines share a common periodicity found to be $\eta_2 = 6.00 \pm 0.01$ d that is consistent with older literature determinations of 5.8–6.1 d for the stellar rotation period (Percy et al. 2010; Artemenko, Grankin & Petrov 2012; Robinson et al. 2022; Bouvier et al. 2023). The RV periodicity is however slightly lower than our previous estimate from B_ℓ measurements (of $6.03^{+0.03}_{-0.04}$ d), which is similar to what was reported for other CTTSs observed with SPIRou (e.g. CI Tau and TW Hya, Donati et al. 2024a, b) and likely results from weak levels of surface differential rotation at the surface of GM Aur. One notable difference between both GP models is that the GP RV curve from atomic lines has a semi-amplitude of 0.33 km s^{-1}, whereas that from CO lines features a lower semi-amplitude of 0.24 km s^{-1}. The difference can be attributed to magnetic fields inducing dominant profile distortions in atomic lines (but not in the magnetically insensitive CO lines) and brightness features generating only weaker perturbations (in both atomic and CO lines). Note that η_3 and η_4 were fixed to their optimal values obtained in the GP analysis of the B_ℓ data (Section 4), as the limited coverage of our observations does not effectively constrain these parameters from the noisier RV data.

As we detect residual power in the filtered RVs around a period of 8.75 d (corresponding to a false alarm probability, FAP $\sim$ 0.2 per cent), we launched a new MCMC run, including this time an RV signal induced by a putative close-in planet on a circular orbit – i.e. with three more parameters being fitted in the GP model: the planet semi-amplitude, orbital period, and time of inferior conjunc-

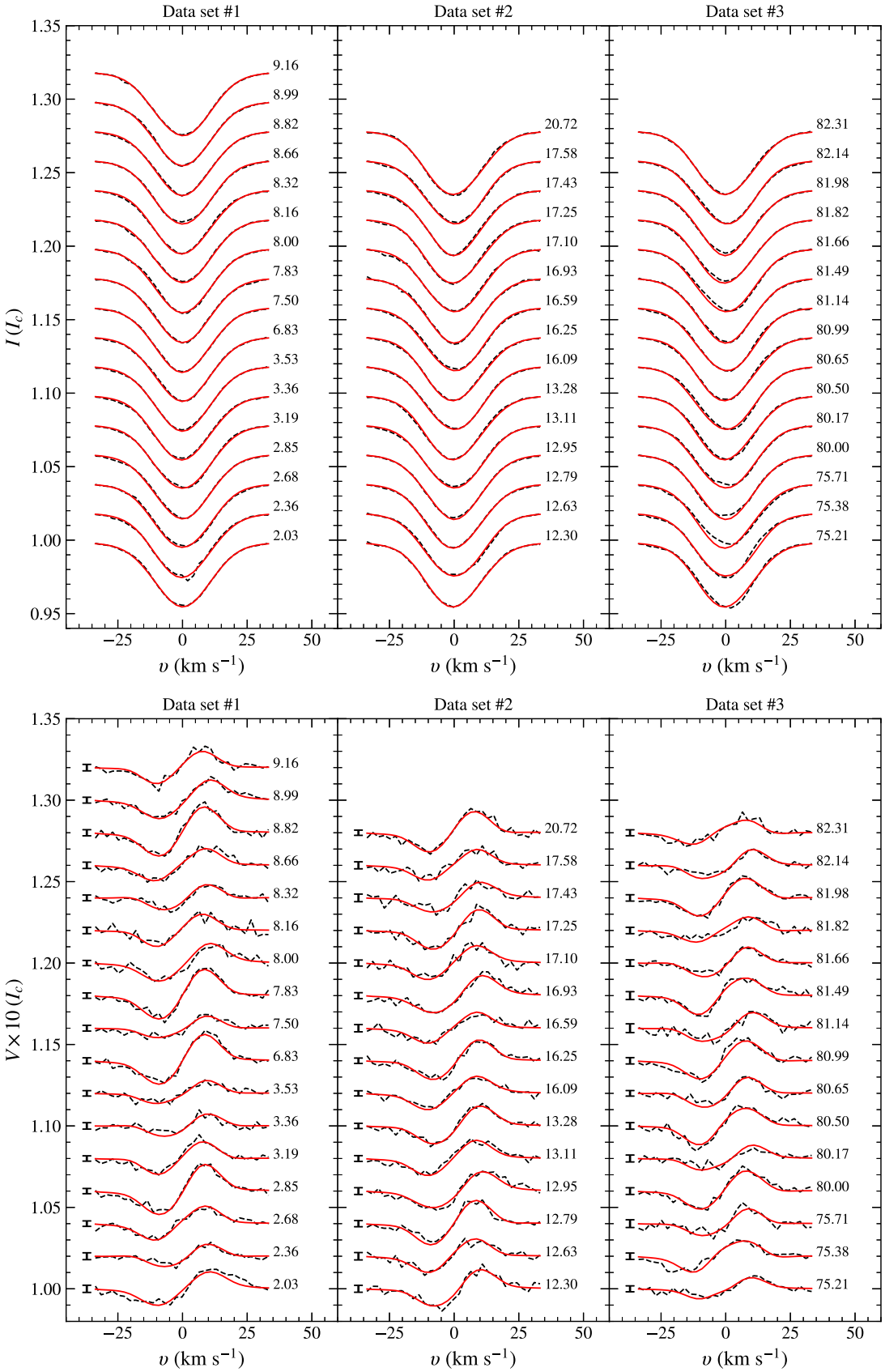

Figure 4. Maximum entropy fit to the Stokes I (first row) and V (second row) LSD observations (dashed black lines). Columns show the ZDI fit (red lines) to the data sets #1, #2, and #3, respectively. Stokes I and V profiles have been vertically shifted for display purposes. Rotation cycles and 1σ error bars (only for the Stokes V profiles) are shown next to each profile.

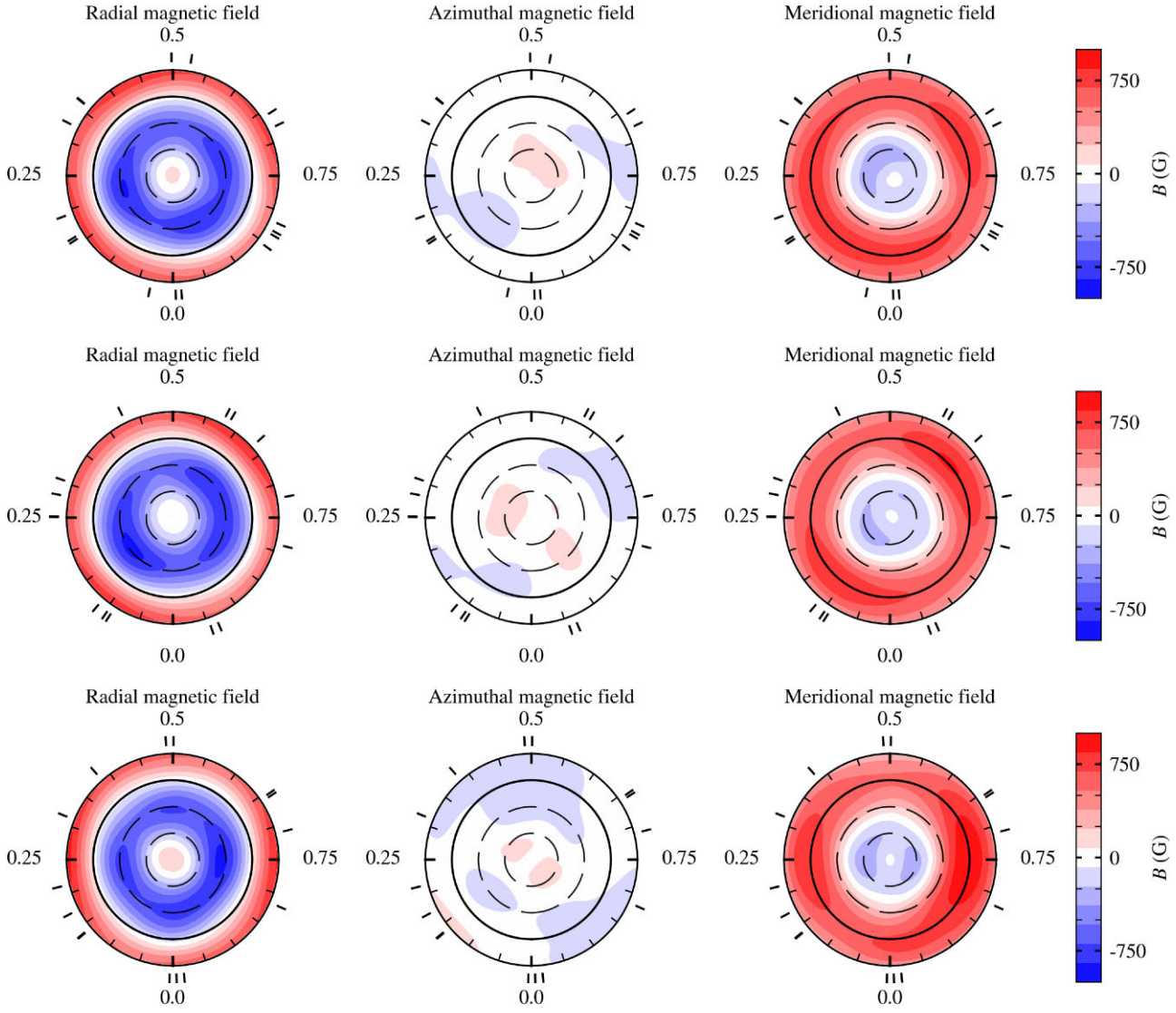

Figure 5. Magnetic field maps of GM Aur reconstructed using data set #1 (top panels), data set #2 (middle panels), and data set #3 (bottom panels). Maps are shown in flattened polar projection in which concentric circles represent 30° steps in latitude. Columns show, respectively, the radial, azimuthal, and meridional components of the magnetic field. Magnetic fields are given in units of Gauss with positive values represented in red shades and negative values in blue.

Table 3. Magnetic field properties of GM Aur derived with ZDI using data set #1 (second column), data set #2 (third column), and data set #3 (fourth column).

Magnetic field properties	Data set #1	Data set #2	Data set #3
$B_{\rm max}$ (G)	880	900	980
$E_{\rm Pol}$ ($E_{\rm Tot}$)	99 per cent	99 per cent	98 per cent
$E_{\rm Tor}$ ($E_{\rm Tot}$)	1 per cent	1 per cent	2 per cent
$E_{\rm Dip}$ ($E_{\rm Pol}$)	65 per cent	65 per cent	62 per cent
$E_{\rm Quad}$ ($E_{\rm Pol}$)	1 per cent	1 per cent	1 per cent
$E_{\rm Oct}$ ($E_{\rm Pol}$)	33 per cent	33 per cent	36 per cent
Pol. axisymmetric ($E_{\rm Pol}$)	98 per cent	98 per cent	96 per cent
$B_{\rm Dip}$ (G)	740	750	705
β (°)	15	10	10
Rotation phase of tilted dipole	0.91	0.95	0.81

tion. The results of both fits (with and without planet) are listed in Table 4. We find a significant RV signal present in the activity-filtered data at a 5.5σ level (Fig. 6), featuring a semi-amplitude of 0.11 ± 0.02 km s^{-1} and an orbital period of 8.745 ± 0.009 d. The detected RV signal is supported by the log-Bayes factor (or log-marginal likelihood increase) of 16.8–i.e. well above the minimal detection threshold of 5 suggested by Jeffreys (1983). Using the GP model with a planet to compute the activity-filtered RVs reveals a periodic signal around 8.745 d (see Fig. C2) that is consistent with the residual power seen in the activity only GP model.

If attributed to a candidate planet, the detected signal would imply a minimum planet mass of $M_b \sin i = 1.10 \pm 0.30\, M_{\rm Jup}$, and a planet mass of $M_b = 1.38 \pm 0.37\, M_{\rm Jup}$ if the planet orbits in the plane of the disc. Fig. 7 shows the phase-folded activity-filtered RV curve obtained in our modelling for both atomic and CO lines. The posterior distributions obtained in the 8-parameter fit to the joint RV data from atomic lines and CO lines are illustrated in Fig. C1. As evidenced by the stacked periodogram in Fig. C3, the RV signal power-detection

Table 4. MCMC results for the joint modelling of the RV data from atomic and CO lines of GM Aur. Results correspond to the GP models with and without planet. Note that the values of η_2, η_3, and η_4 are shared in the GPs of atomic and CO lines.

Parameters	Name	GP model values	GP + Planet model values	Prior
GP semi-amplitude of the atomic lines ($km\,s^{-1}$)	η_1 (atomic lines)	$0.33^{+0.07}_{-0.05}$	$0.32^{+0.06}_{-0.05}$	$\mathcal{U}(0, 100)$
GP semi-amplitude of the CO lines ($km\,s^{-1}$)	η_1 (CO lines)	$0.24^{+0.06}_{-0.04}$	$0.23^{+0.05}_{-0.04}$	$\mathcal{U}(0, 100)$
Rotation period (d)	η_2	6.00 ± 0.01	5.99 ± 0.01	$\mathcal{N}(6.04, 1)$
Decay time scale (d)	η_3	97	97	Fixed
Smoothing factor	η_4	0.33	0.33	Fixed
White noise of the atomic lines ($km\,s^{-1}$)	η_5 (atomic lines)	0.06 ± 0.03	0.00 ± 0.05	$\mathcal{U}(-100, 100)$
White noise of the CO lines ($km\,s^{-1}$)	η_5 (CO lines)	0.09 ± 0.03	0.00 ± 0.05	$\mathcal{U}(-100, 100)$
Orbital semi-amplitude ($km\,s^{-1}$)	K_b		0.11 ± 0.02	$\mathcal{U}(0, 1)$
Orbital period (d)	P_b		8.745 ± 0.009	$\mathcal{N}(8.75, 0.1)$
Time of inferior conjunction (+ 2459000)	BJD_b		704.0 ± 0.5	$\mathcal{N}(703.8, 2)$
Minimum planet mass (M_{Jup})	$M_b \sin i$		1.10 ± 0.30	Derived from K_b, P_b, and $M_\star$
Reduced-χ^2	χ^2_r	1.07	0.61	
RMS of atomic lines ($km\,s^{-1}$)	RMS (atomic lines)	0.091	0.076	
RMS of CO lines ($km\,s^{-1}$)	RMS (CO lines)	0.113	0.079	
Marginal log-likelihood	$\log \mathcal{L}_M$	21.7	38.5	
log-Bayes factor [a]	$\log BF = \Delta \log \mathcal{L}_M$	0.0	16.8	

[a]The Bayes factor is computed with respect to the reference model without a planet.

increases with the number of observations, which is expected for planet-induced signals. We also investigated whether an eccentric orbit yields a better fit than a circular orbit to our RV data, and found an eccentricity consistent with 0 (with an error bar of ± 0.05), along with a non-significant change in marginal likelihood (with respect to the circular case), supporting our initial assumption of a circular orbit.

We double-checked that the orbital solutions obtained through an independent fit to the RV data from atomic and CO lines are in good agreement with the solution obtained from the joint modelling of both sets of lines, although with lower Bayesian evidence (of 6.2 and 11.5 for atomic lines and CO lines, respectively). This result tells in particular that the detected RV signal shows up in the whole spectrum and on all spectral lines (as expected from, e.g. a planet RV signal), and not just in one single set of lines or spectral band (if caused by, e.g. activity or a non-axisymmetric inner disc structure). Tables 5 and 6 present the GP results obtained in the individual fit to the RV data from atomic and CO lines, respectively.

Furthermore, it is unlikely that the candidate planet would drive a pulsed accretion mechanism in GM Aur given its circular orbit (Artymowicz & Lubow 1996). In agreement with this, a quick inspection of previously published TESS data does not show significant power at the orbital period.

7 SUMMARY AND DISCUSSION

We analyzed nIR spectra of the CTTS GM Aur, collected with the SPIRou spectropolarimeter at CFHT from 2021 September to 2023 January. We computed Stokes I and V LSD profiles for the 49 collected spectra. Focusing first on the temporal analysis of the surface longitudinal magnetic field, we detected a quasi-periodic signal with a periodicity of $6.03^{+0.03}_{-0.04}$ d. This agrees with the range of stellar rotation periods documented in the literature, going from 5.8 to 6.1 d, as determined through spectroscopy and photometry (Percy et al. 2010; Robinson et al. 2022; Bouvier et al. 2023).

The primary aim of our investigation was to recover the large-scale surface magnetic field of GM Aur and investigate its magnetospheric accretion regime. To accomplish that, we analysed the LSD profiles using ZDI, dividing our data into three distinct sets, assuming that surface brightness (i.e. temperature) inhomogeneities and/or large-scale magnetic fields remained static within each set.

7.1 The large-scale magnetic field topology

The reconstructed large-scale magnetic field of GM Aur revealed a topology predominantly characterized by a dipolar configuration that is slightly tilted towards rotational phases 0.81–0.95. The dipole tilt angles obtained in our study (10° and 15°) agree with the small value reported in November 2011 by McGinnis et al. (2020), who inferred a tilt angle $\beta = 13^{\circ}{}^{+16^{\circ}}_{-13^{\circ}}$ through the analysis of the variability of the optical accretion line HeI 587.6 nm. The average field strength of this dipole is about 730 G, close to those of other CTTSs with similar stellar rotation periods like, e.g. V2129 Oph (of 625 G, Donati et al. 2007, 2011a). Indeed, a positive correlation between B_{Dip} and P_{rot} has been reported in the literature for CTTS and taken as a natural consequence of star–disc interaction torques (Johnstone et al. 2014; Vidotto et al. 2014; Amard & Matt 2023), in which the magnetospheric interaction with the circumstellar disc sets the stellar rotation period. Combining the peak magnetic field at the stellar surface with the magnetic filling factor of about 40 per ent suggests that the small-scale field may locally reach strengths up to 2.5 kG, consistent with previous small-scale field measurements from Zeeman broadening of the atomic lines of GM Aur (Johns-Krull 2007; Flores et al. 2022).

Our ZDI analysis showed that magnetic effects can alone explain the modulation of the Stokes I and V LSD profiles of atomic lines without the need for brightness inhomogeneities. Indeed, the Stokes I profiles show the most significant distortions in the latest observations when the maximum magnetic field strength is about 100 G larger than in the latest epochs (see Fig. 4). Brightness inhomogeneities are none the less present at the surface of the star (hence the activity jitter in the RV curve of the magnetically insensitive CO lines, see Section 6), but are found to generate profile distortions in atomic lines smaller than those from magnetic fields. Nevertheless, the companion study conducted by Bouvier et al. (2023) demonstrated the existence of an accretion spot positioned at rotational phase 0 during the same period of our observations (concomitant to the first two data sets). We argue that this discrepance

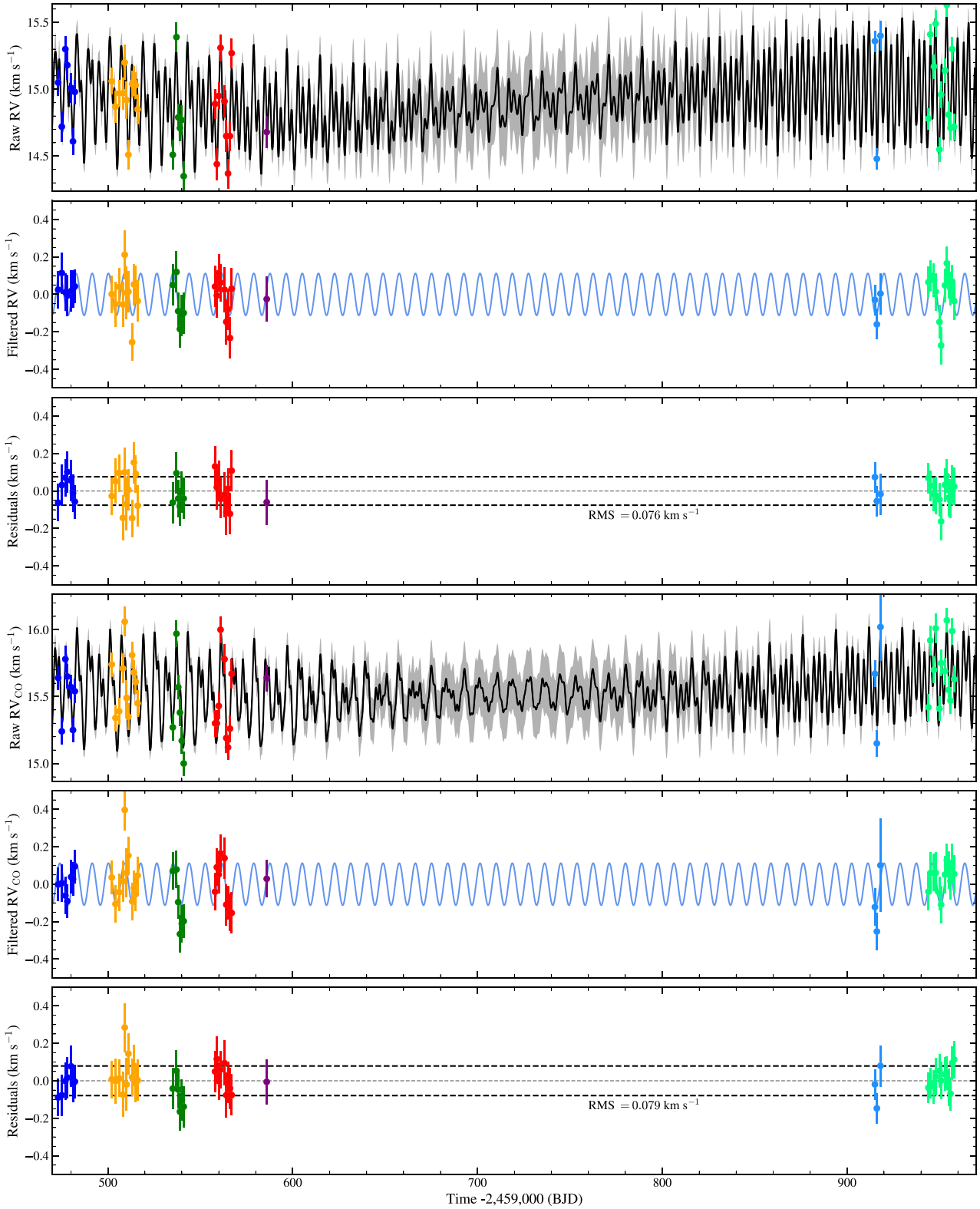

Figure 6. Joint GP regression of the raw RVs from both atomic lines (first 3 rows) and CO lines (last 3 rows) of GM Aur. Rows 1 and 4 illustrate the raw RVs alongside the GP + Planet model prediction. Rows 2 and 5 show to the activity-filtered RV data and the modelled planetary RV signal (blue curve). Rows 3 and 6 give activity- and planet-filtered RV residuals. Symbol colours carry the same meaning as in Fig. 3.

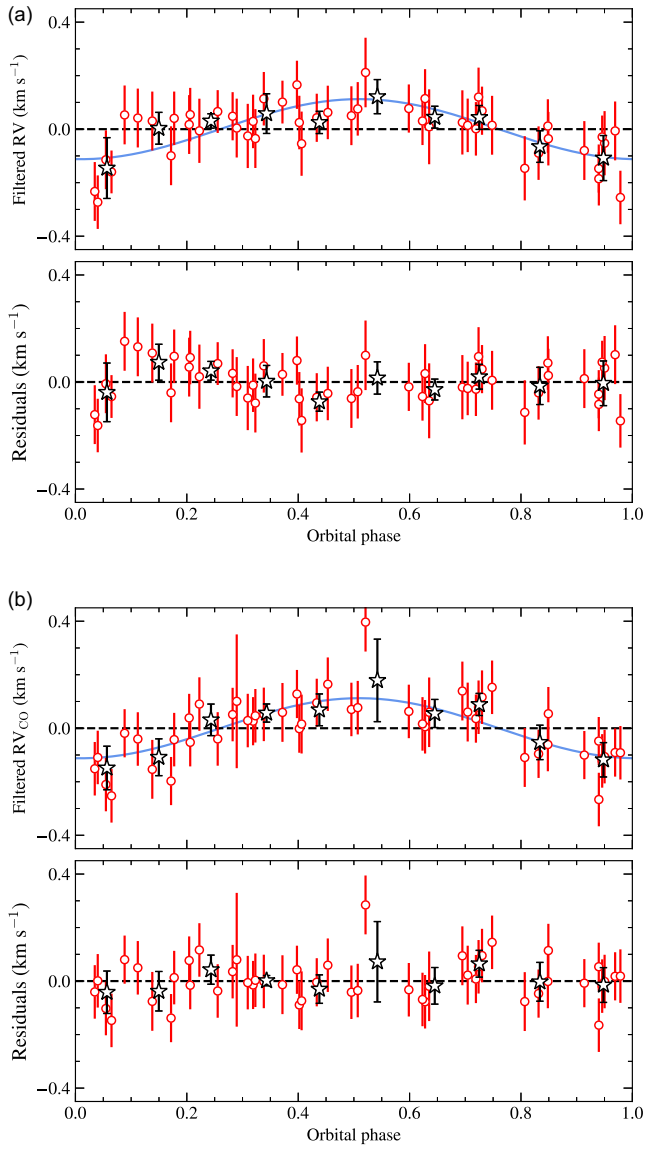

Figure 7. Activity-filtered and residual RV data of GM Aur, respectively for atomic lines (a) and for CO lines (b), phase-folded on the 8.745 d orbital period. Red points illustrate the RVs, whereas black stars correspond to averaged values over 0.1 phase bins. The blue sinusoid is the result of the combined MCMC fit to both atomic and CO lines.

most likely arises because we are blind to the accretion spot in the nIR domain, which is defined by typical temperatures of about 8000 K (Hartmann et al. 2016). Previous optical studies have resorted to accretion-powered emission lines to gather more information about the hot spot and precisely pinpoint its location at the stellar surface (e.g. Donati et al. 2010b, 2013). Unfortunately, we are unable to employ a similar procedure with our data as there is no clear accretion proxy that solely probes the accretion spot at the footpoint of accretion funnels in the nIR domain, but rather accretion proxies that carry information from all over the accretion funnel and inner disc regions (e.g. Sousa et al. 2023). Contemporaneous nIR and optical spectropolarimetry would be required to draw a picture of the surface brightness distribution of GM Aur in future observations. Last but not least, we note that the large-scale field of GM Aur is tilted towards phase 0.9. This is in rough agreement with the result of Bouvier et al. (2023) reporting that the accretion column (and the chromospheric hot spot at the base of the accretion funnel) is apparently anchored/located at the surface of GM Aur near phase 0.0.

In a broader context, the magnetic topology of GM Aur supports the work of other studies in this area, linking the magnetic field complexity with the stellar internal structure (e.g. Gregory et al. 2012). Fig. 8 compares the large-scale magnetic field morphology of CTTS at different locations in the Hertzsprung–Russel diagram. This figure shows that the dominant axisymmetric poloidal field of GM Aur resembles the magnetic configuration of CTTS with either a small radiative core or a fully convective structure (e.g. AA Tau, BP Tau, and DN Tau). GM Aur's simple large-scale magnetic field morphology translates in a dipole-to-octupole ratio of about 2 at all epochs. This result reinforces that the reconstructed magnetic maps of GM Aur differ mainly because of the magnetic excursion of the dipolar field component. The minor rearrangement of the field configuration is likely what causes the short-term variability seen in the B_ℓ data. These results hint towards a non-stationary dynamo state, although a clear picture can only be obtained through regular magnetic monitoring of GM Aur. We emphasize that future analogous works modelling the magnetic field of other CTTSs are of paramount importance to get statistically significant correlations between the magnetic field morphology and the evolutionary stage of stars.

7.2 GM Aur's magnetospheric accretion regime

Previous theoretical investigations have highlighted the significance of the relative positions of the disc corotation radius ($r_{\rm cor}$) and the disc truncation radius ($r_{\rm m}$) in determining the type of stellar accretion regime (e.g. Blinova, Romanova & Lovelace 2016; Romanova et al. 2018). Based on the polar field strength $B_{\rm Dip}$ derived from the magnetic topologies obtained in this study and considering the accretion rate of $(0.5 \pm 0.4) \times 10^{-8} {\rm M}_\odot {\rm yr}^{-1}$ from the Hβ line flux (Bouvier et al. 2023), an estimation of the magnetospheric truncation radius can be made using the analytical solution proposed by Bessolaz et al. (2008):

$$\frac{r_{\rm m}}{R_\star} = 2 m_s^{2/7} \left(\frac{B_{\rm Dip}}{280\,G}\right)^{4/7} \left(\frac{\dot{M}_{\rm acc}}{10^{-8}{\rm M}_\odot{\rm yr}^{-1}}\right)^{-2/7} \times \left(\frac{M_\star}{0.8{\rm M}_\odot}\right)^{-1/7} \left(\frac{R_\star}{2R_\odot}\right)^{5/7} \quad (7)$$

where $m_s \approx 1$ is the sonic Mach number, $\dot{M}_{\rm acc}$ is the mass accretion rate, and $B_{\rm Dip}$ is the dipole field strength at the pole (roughly taken as the mean value from the dipolar field strengths reported in Table 3). Utilizing this equation, the magnetosphere is predicted to truncate the circumstellar disc of GM Aur at an approximate value of $r_{\rm m} = 4.1 \pm 1.0\,{\rm R}_\star$ (0.039 ± 0.009 au). Furthermore, assuming Keplerian rotation for the inner disc of GM Aur, as suggested by the CO emission from the disc (e.g. Dutrey et al. 1998; Simon, Dutrey & Guilloteau 2000; Hughes et al. 2013), the radius at which the angular velocity of the disc matches that of the star can be computed as

$$r_{\rm cor} = \left(\frac{GM_\star}{\Omega_\star^2}\right)^{1/3}, \quad \text{where} \quad \Omega_\star = \frac{v_{\rm eq}\,\sin i}{R_\star \sin i}. \quad (8)$$

This relationship leads to $r_{\rm cor} = 6.8 \pm 0.2\,{\rm R}_\star$ (0.064 ± 0.002 au).

It is possible to draw a picture of the magnetospheric accretion of GM Aur based on the ratio of $r_{\rm m}/r_{\rm cor}$ equal to 0.60 ± 0.15. This ratio is at the limit of the stable accretion regime (Blinova et al. 2016; Pantolmos, Zanni & Bouvier 2020), and is apparently enough to generate stable accretion in the system, but not to enforce the star to spin down to the longer rotation periods (8–10 d) of prototypical CTTSs such as AA Tau or CI Tau (Donati et al. 2010b, 2020a).

Table 5. Similar to Table 4, but for the RV data from atomic lines of GM Aur.

Parameters	Name	GP model values	GP + Planet model values	Prior
GP semiamplitude ($\mathrm{km\,s^{-1}}$)	η_1	$0.33^{+0.07}_{-0.05}$	$0.32^{+0.07}_{-0.05}$	$\mathcal{U}(0, 100)$
Rotation period (d)	η_2	6.00 ± 0.02	5.99 ± 0.02	$\mathcal{N}(6.04, 1)$
Decay time-scale (d)	η_3	97	97	Fixed
Smoothing factor	η_4	0.33	0.33	Fixed
White noise ($\mathrm{km\,s^{-1}}$)	η_5	0.06 ± 0.03	0.00 ± 0.05	$\mathcal{U}(-100, 100)$
Orbital semiamplitude ($\mathrm{km\,s^{-1}}$)	K_b		0.09 ± 0.03	$\mathcal{U}(0, 1)$
Orbital period (d)	P_b		$8.74^{+0.02}_{-0.03}$	$\mathcal{N}(8.75, 0.1)$
Time of inferior conjunction (+2459000)	BJD_b		704 ± 1	$\mathcal{N}(703.8, 2)$
Minimum planet mass (M_{Jup})	$M_b \sin i$		0.85 ± 0.30	Derived from K_b, P_b, and $M_\star$
Reduced-χ^2	χ^2_r	0.86	0.58	
Residuals root-mean-square ($\mathrm{km\,s^{-1}}$)	RMS	0.091	0.074	
Marginal log-likelihood	$\log \mathcal{L}_M$	10.5	16.7	
log-Bayes factor	$\log \mathrm{BF} = \Delta \log \mathcal{L}_M$	0.0	6.2	

Table 6. Similar to Table 4, but for the RV data from CO lines of GM Aur.

Parameters	Name	GP model values	GP + planet model values	Prior
GP semi-amplitude ($\mathrm{km\,s^{-1}}$)	η_1	$0.24^{+0.06}_{-0.04}$	$0.23^{+0.05}_{-0.04}$	$\mathcal{U}(0, 100)$
Rotation period (d)	η_2	$6.00^{+0.03}_{-0.02}$	5.99 ± 0.02	$\mathcal{N}(6.04, 1)$
Decay time-scale (d)	η_3	97	97	Fixed
Smoothing factor	η_4	0.33	0.33	Fixed
White noise ($\mathrm{km\,s^{-1}}$)	η_5	0.09 ± 0.03	0.00 ± 0.05	$\mathcal{U}(-100, 100)$
Orbital semi-amplitude ($\mathrm{km\,s^{-1}}$)	K_b		0.13 ± 0.03	$\mathcal{U}(0, 1)$
Orbital period (d)	P_b		8.75 ± 0.01	$\mathcal{N}(8.75, 0.1)$
Time of inferior conjunction (+ 2459000)	BJD_b		$704.1^{+0.7}_{-0.8}$	$\mathcal{N}(703.8, 2)$
Minimum planet mass (M_{Jup})	$M_b \sin i$		1.23 ± 0.30	Derived from K_b, P_b, and $M_\star$
Reduced-χ^2	χ^2_r	1.3	0.66	
Residuals root-mean-square ($\mathrm{km\,s^{-1}}$)	RMS	0.113	0.078	
Marginal log-likelihood	$\log \mathcal{L}_M$	11.2	22.7	
log-Bayes factor	$\log \mathrm{BF} = \Delta \log \mathcal{L}_M$	0.0	11.5	

This conclusion is supported by the long-lived accretion pattern reported by Bouvier et al. (2023), who analysed photometric and spectroscopic data covering 30 rotational cycles.

Given this low value of $r_{\mathrm{m}}/r_{\mathrm{cor}}$, we speculate that GM Aur may switch at times to an unstable accretion regime, perhaps explaining the quasi-periodic nature of its light curve and the existence of accretion bursts reported in the literature (Robinson & Espaillat 2019; Robinson et al. 2022; Wendeborn et al. 2024b). Past studies have identified that it is not uncommon for CTTSs to change their accretion behaviour, as seen in NGC 2264 (McGinnis et al. 2015; Sousa et al. 2016). These transitions in the accretion regime could be associated with the onset or efficiency of the Rayleigh–Taylor instability that occurs at the interface between the accretion disc and the magnetosphere, which depends on the strength and orientation of the magnetic field (Kurosawa & Romanova 2013). Nevertheless, we cannot exclude the possibility that a variable inner disc density contributes to (or even dictates) the changes in mass accretion rate and the quasi-periodic nature of GM Aur's light curve (Espaillat et al. 2019). These results further justify monitoring the magnetic field of GM Aur over the next years.

7.3 Detection of a RV signal

We obtained RV measurements from the Stokes I LSD profiles computed from either a photospheric atomic line mask or a CO bandhead line mask. Fitting the time-series data with a Gaussian Process revealed a residual signal in the activity-filtered RVs from atomic and CO lines, detected at a 5.5σ level. The signal has a semi-amplitude of $0.11 \pm 0.02\,\mathrm{km\,s^{-1}}$ and a periodicity of 8.745 ± 0.009 d, and potentially reflects the presence of a candidate planet on a circular orbit. The competing GP models (with or without planet) showed significant Bayesian evidence for the detected RV signal, with an increase in the marginal log-likelihood of $\Delta \log \mathcal{L}_M = 16.8$.

Moreover, we find that the significance of the reported RV signal increases with the number of RV data points considered (see Fig. C3), consistent with what would be expected from a candidate planetary companion orbiting GM Aur (Mortier & Collier Cameron 2017). We also confirmed that the orbital parameters obtained in the GP fit of the RV data from atomic and CO lines fitted independently agree within 1σ with the solution obtained from both sets of lines. However, these models have lower Bayesian evidence for the planet detection (of 6.2 and 11.5) due to the smaller amount of information used in the GP regression.

In conclusion, our research has provided compelling evidence of a candidate newborn giant planet orbiting GM Aur. If attributed to a candidate planet, the detected RV signal would imply a minimum planet mass of $1.10 \pm 0.30\,M_{\mathrm{Jup}}$, and a planet mass of $1.38 \pm 0.37\,M_{\mathrm{Jup}}$ if the planet orbits in the plane of the disc. It would imply that this candidate planet orbits at a distance of 0.082 ± 0.002 au ($8.74 \pm 0.32\,R_\star$), located within the inner accretion

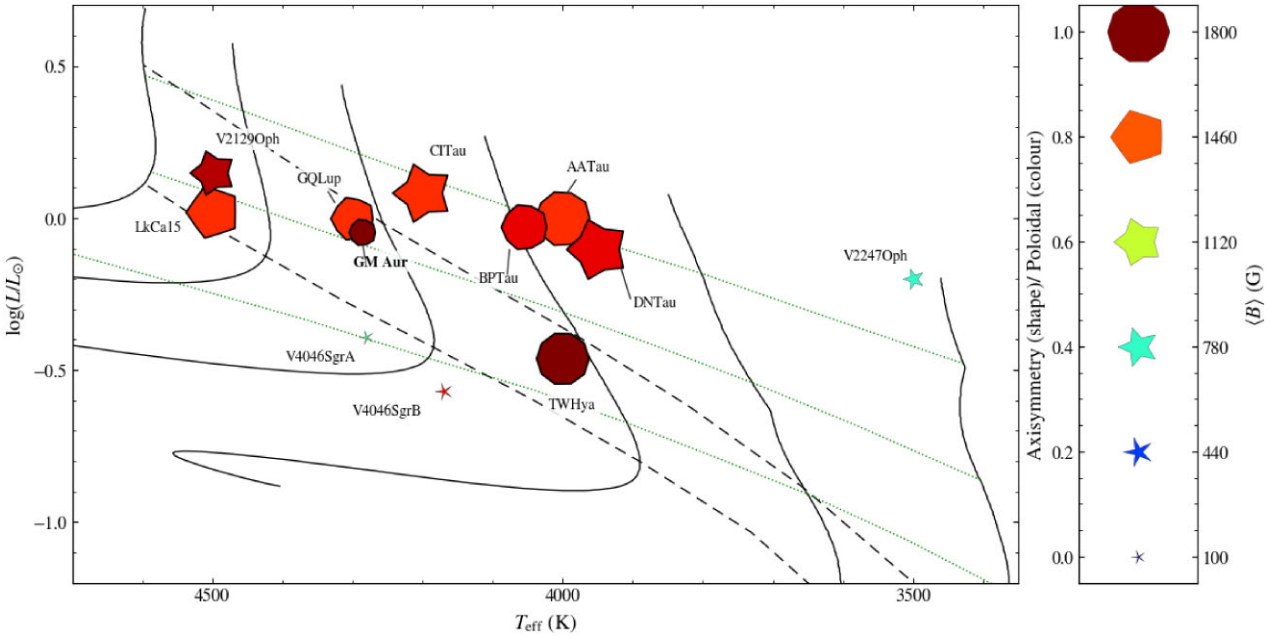

Figure 8. Magnetic Hertzsprung–Russell diagram for CTTS. Symbols depict the properties of the large-scale magnetic field reconstructed for each star; symbol sizes are proportional to the averaged field strength ($\langle B \rangle$), colours represent the field configuration (from red to blue for purely poloidal to purely toroidal fields), and shapes illustrate the degree of axisymmetry of the poloidal field component (with higher axisymmetry shown as a more circular symbol). Evolutionary models are similar to Fig. 1. Mass tracks go from 0.3 to 1.3 $M_\odot$ in steps of 0.2 $M_\odot$ (black lines) and isochrones are for ages of 1, 5, and 10 Myr (dotted green lines).

disc, slightly beyond the corotation radius. This makes GM Aur b one of the very few close-in candidate planets currently identified around CTTSs (e.g. Manick et al. 2024; Donati et al. 2024a). Finally, it is unlikely that a single planet can carve the large dust cavity observed in GM Aur (∼ 40 au). The odds are that multiple planets exist within the dust gap of GM Aur, as observed for other stars with large dust cavities such as the CTTS PDS 70 (Haffert et al. 2019). Further observations are needed to firmly confirm the planetary nature of the RV signal uncovered in this study and to characterize the planet's atmospheric properties, providing us with an ideal opportunity to derive observational constraints for theoretical models of the formation and evolution of close-in giant planets.

ACKNOWLEDGEMENTS

We thank the anonymous referee for helping improve and clarify the paper. BZ acknowledges funding from the CAPES-PrInt program (#88887.683070/2022-00 and #88887.802913/2023-00). BZ and SHPA acknowledge financial support from CNPq, CAPES, and FAPEMIG (APQ-01033-22). JFD, BZ, and CM acknowledge funding from the European Research Council (ERC) under the H2020 research & innovation programme (grant agreement #740651 NewWorlds). JB acknowledges funding from ERC (grant agreement #742095 SPIDI). AC acknowledge funding from the French ANR under contract number ANR18CE310019 (SPlaSH). This work is supported by the French National Research Agency in the framework of the Investissements d'Avenir program (ANR-15-IDEX-02), through the funding of the 'Origin of Life' project of the Grenoble-Alpes University.

This paper is based on observations obtained at CFHT which is operated by the National Research Council of Canada, the Institut National des Sciences de l'Univers of the Centre National de la Recherche Scientique of France, and the University of Hawaii. The observations at the CFHT were performed with care and respect from the summit of Maunakea which is a significant cultural and historic site.

DATA AVAILABILITY

This paper includes data collected by the SPIRou spectropolarimeter taken as part of the CFHT Large Programs SLS and SPICE (program IDs: 21BP42 & 22BP45). The SLS data are already publicly available from the Canadian Astronomy Data Center, whereas the SPICE data will become available by the second semester of 2025.

REFERENCES

Alencar S. H. P. et al., 2012, A&A, 541, A116
Amard L., Matt S., 2023, A&A, 678, A7
Angus R., Morton T., Aigrain S., Foreman-Mackey D., Rajpaul V., 2018, MNRAS, 474, 2094
Artemenko S. A., Grankin K. N., Petrov P. P., 2012, Astron. Lett., 38, 783
Artymowicz P., Lubow S. H., 1996, ApJ, 467, L77
Baraffe I., Homeier D., Allard F., Chabrier G., 2015, A&A, 577, A42
Bellotti S. et al., 2023, A&A, 676, A56
Bertout C., Genova F., 2006, A&A, 460, 499
Bessolaz N., Zanni C., Ferreira J., Keppens R., Bouvier J., 2008, A&A, 478, 155
Blinova A. A., Romanova M. M., Lovelace R. V. E., 2016, MNRAS, 459, 2354
Bohn A. J. et al., 2022, A&A, 658, A183
Bosman A. D. et al., 2021, ApJS, 257, 15
Bouvier J. et al., 2007, A&A, 463, 1017
Bouvier J., Matt S. P., Mohanty S., Scholz A., Stassun K. G., Zanni C., 2014, in Beuther H., Klessen R. S., Dullemond C. P., Henning T., eds, Protostars and Planets VI. Univ. Arizona Press, Tucson, p. 433
Bouvier J. et al., 2020, A&A, 643, A99
Bouvier J. et al., 2023, A&A, 672, A5
Brown S. F., Donati J. F., Rees D. E., Semel M., 1991, A&A, 250, 463

Brun A. S., Strugarek A., Noraz Q., Perri B., Varela J., Augustson K., Charbonneau P., Toomre J., 2022, ApJ, 926, 21
Calvet N. et al., 2005, ApJ, 630, L185
Christensen U. R., 2010, Space Sci. Rev., 152, 565
Cook N. J. et al., 2022, PASP, 134, 114509
D'Orazi V., Biazzo K., Randich S., 2011, A&A, 526, A103
Donati J. F., Brown S. F., 1997, A&A, 326, 1135
Donati J. F., Semel M., Carter B. D., Rees D. E., Collier Cameron A., 1997, MNRAS, 291, 658
Donati J. F. et al., 2006, MNRAS, 370, 629
Donati J. F. et al., 2007, MNRAS, 380, 1297
Donati J. F. et al., 2008, MNRAS, 386, 1234
Donati J. F. et al., 2010a, MNRAS, 402, 1426
Donati J. F. et al., 2010b, MNRAS, 409, 1347
Donati J. F. et al., 2011a, MNRAS, 412, 2454
Donati J. F. et al., 2011b, MNRAS, 417, 472
Donati J. F. et al., 2011c, MNRAS, 417, 1747
Donati J. F. et al., 2012, MNRAS, 425, 2948
Donati J. F. et al., 2013, MNRAS, 436, 881
Donati J. F. et al., 2017, MNRAS, 465, 3343
Donati J. F. et al., 2019, MNRAS, 483, L1
Donati J. F. et al., 2020a, MNRAS, 491, 5660
Donati J. F. et al., 2020b, MNRAS, 498, 5684
Donati J. F. et al., 2023a, MNRAS, 525, 455
Donati J. F. et al., 2023b, MNRAS, 525, 2015
Donati J. F. et al., 2024a, MNRAS, 530, 264
Donati J. F. et al., 2024b, MNRAS, 531, 3256
Dutrey A., Guilloteau S., Prato L., Simon M., Duvert G., Schuster K., Menard F., 1998, A&A, 338, L63
Edwards S., Fischer W., Hillenbrand L., Kwan J., 2006, ApJ, 646, 319
Emeriau-Viard C., Brun A. S., 2017, ApJ, 846, 8
Espaillat C. C., Macías E., Hernández J., Robinson C., 2019, ApJ, 877, L34
Fares R. et al., 2012, MNRAS, 423, 1006
Finociety B., Donati J. F., 2022, MNRAS, 516, 5887
Finociety B. et al., 2021, MNRAS, 508, 3427
Finociety B. et al., 2023a, MNRAS, 520, 3049
Finociety B. et al., 2023b, MNRAS, 526, 4627
Flores C., Connelley M. S., Reipurth B., Duchêne G., 2022, ApJ, 925, 21
Folsom C. P. et al., 2016, MNRAS, 457, 580
Foreman-Mackey D., Hogg D. W., Lang D., Goodman J., 2013, PASP, 125, 306
Francis L., van der Marel N., 2020, ApJ, 892, 111
Gaia Collaboration, 2021, A&A, 649, A1
Gastine T., Duarte L., Wicht J., 2012, A&A, 546, A19
Goodman J., Weare J., 2010, Commun. Applied Math. Computat. Sci., 5, 65
Gray D. F., 1982, ApJ, 255, 200,
Gregory S. G., Donati J. F., Morin J., Hussain G. A. J., Mayne N. J., Hillenbrand L. A., Jardine M., 2012, ApJ, 755, 97
Guerrero G., Zaire B., Smolarkiewicz P. K., de Gouveia Dal Pino E. M., Kosovichev A. G., Mansour N. N., 2019, ApJ, 880, 6
Gully-Santiago M. A. et al., 2017, ApJ, 836, 200
Gustafsson B., Edvardsson B., Eriksson K., Jørgensen U. G., Nordlund Å., Plez B., 2008, A&A, 486, 951
Haffert S. Y., Bohn A. J., de Boer J., Snellen I. A. G., Brinchmann J., Girard J. H., Keller C. U., Bacon R., 2019, Nat. Astron., 3, 749
Hartigan P., Edwards S., Ghandour L., 1995, ApJ, 452, 736
Hartmann L., Hewett R., Calvet N., 1994, ApJ, 426, 669
Hartmann L., Herczeg G., Calvet N., 2016, ARA&A, 54, 135
Herczeg G. J., Hillenbrand L. A., 2014, ApJ, 786, 97
Hornbeck J. B. et al., 2016, ApJ, 829, 65
Huang J. et al., 2020, ApJ, 891, 48
Hughes A. M., Hull C. L. H., Wilner D. J., Plambeck R. L., 2013, AJ, 145, 115
Hussain G. A. J. et al., 2009, MNRAS, 398, 189
Ingleby L. et al., 2013, ApJ, 767, 112
Ingleby L., Espaillat C., Calvet N., Sitko M., Russell R., Champney E., 2015, ApJ, 805, 149
Izquierdo A. F., Testi L., Facchini S., Rosotti G. P., van Dishoeck E., Wölfer L., Paneque-Carreño T., 2023, A&A, 674, A113
Jeffreys H., 1983, Theory of Probability. Oxford Univ. Press, Oxford
Johns-Krull C. M., 2007, ApJ, 664, 975
Johns-Krull C. M., Valenti J. A., 2001, ApJ, 561, 1060
Johnstone C. P., Jardine M., Gregory S. G., Donati J. F., Hussain G., 2014, MNRAS, 437, 3202
Kochukhov O., 2021, A&AR, 29, 1,
Kurosawa R., Romanova M. M., 2013, MNRAS, 431, 2673
Landi Degl'Innocenti E., Landolfi M., 2004, Polarization in Spectral Lines. Astrophysics and Space Science Library, Vol. 307. Springer, Dordrecht
Lehmann L. T., Donati J. F., 2022, MNRAS, 514, 2333
López-Valdivia R. et al., 2021, ApJ, 921, 53
Luhman K. L., 2018, AJ, 156, 271
Macías E. et al., 2018, ApJ, 865, 37
Manara C. F., Testi L., Natta A., Rosotti G., Benisty M., Ercolano B., Ricci L., 2014, A&A, 568, A18
Manick R. et al., 2024, A&A, 686, A249,
McGinnis P. T. et al., 2015, A&A, 577, A11
McGinnis P., Bouvier J., Gallet F., 2020, MNRAS, 497, 2142
Morin J. et al., 2008, MNRAS, 390, 567
Morin J., Donati J. F., Petit P., Delfosse X., Forveille T., Jardine M. M., 2010, MNRAS, 407, 2269
Mortier A., Collier Cameron A., 2017, A&A, 601, A110,
Muzerolle J., Calvet N., Hartmann L., 2001, ApJ, 550, 944
Nelissen M., McGinnis P., Rangaswamy D., Folsom C., Ray T., 2021, The 20.5th Cambridge Workshop on Cool Stars, Stellar Systems, and the Sun (CS20.5). Zenodo, available at: https://zenodo.org/records/4567157
Nelissen M. et al., 2023, A&A, 670, A165
Netzel C., 2018, Astron. Nachr., 339, 101
Nofi L. A. et al., 2021, ApJ, 911, 138
Nowacki H. et al., 2023, A&A, 678, A86
Pantolmos G., Zanni C., Bouvier J., 2020, A&A, 643, A129
Percy J. R., Grynko S., Seneviratne R., Herbst W., 2010, PASP, 122, 753
Petit P. et al., 2021, A&A, 648, A55,
Piskunov N. E., Kupka F., Ryabchikova T. A., Weiss W. W., Jeffery C. S., 1995, A&AS, 112, 525
Pouilly K. et al., 2020, A&A, 642, A99
Pouilly K. et al., 2021, A&A, 656, A50
Pouilly K., Kochukhov O., Kóspál Á., Hahlin A., Carmona A., Ábrahám P., 2023, MNRAS, 518, 5072
Raynaud R., Petitdemange L., Dormy E., 2015, MNRAS, 448, 2055
Rice W. K. M., Wood K., Armitage P. J., Whitney B. A., Bjorkman J. E., 2003, MNRAS, 342, 79
Robinson C. E., Espaillat C. C., 2019, ApJ, 874, 129
Robinson C. E., Espaillat C. C., Rodriguez J. E., 2022, ApJ, 935, 54
Romanova M. M., Blinova A. A., Ustyugova G. V., Koldoba A. V., Lovelace R. V. E., 2018, New A, 62, 94,
Salyk C., Blake G. A., Boogert A. C. A., Brown J. M., 2009, ApJ, 699, 330
Semel M., 1989, A&A, 225, 456
Simon M., Dutrey A., Guilloteau S., 2000, ApJ, 545, 1034
Simon M. et al., 2017, ApJ, 844, 158
Skilling J., Bryan R. K., 1984, MNRAS, 211, 111
Sokal K. R., Johns-Krull C. M., Mace G. N., Nofi L., Prato L., Lee J.-J., Jaffe D. T., 2020, ApJ, 888, 116
Sousa A. P. et al., 2016, A&A, 586, A47
Sousa A. P. et al., 2023, A&A, 670, A142
Stelzer B., Neuhäuser R., 2001, A&A, 377, 538
Strassmeier K. G., Carroll T. A., Ilyin I. V., 2023, A&A, 674, A118
Strom K. M., Strom S. E., Edwards S., Cabrit S., Skrutskie M. F., 1989, AJ, 97, 1451
Vidotto A. A. et al., 2014, MNRAS, 441, 2361
Wendeborn J. et al., 2024a, ApJ, 970, 118
Wendeborn J. et al., 2024b, ApJ, 971, 96
Yadav R. K., Christensen U. R., Morin J., Gastine T., Reiners A., Poppenhaeger K., Wolk S. J., 2015, ApJ, 813, L31
Yu L. et al., 2017, MNRAS, 467, 1342,

Zaire B., Guerrero G., Kosovichev A. G., Smolarkiewicz P. K., Landin N. R., 2016, Proc. Int. Astron. Union, 12, 30
Zaire B., Donati J. F., Klein B., 2021, MNRAS, 504, 1969
Zaire B., Donati J. F., Klein B., 2022a, MNRAS, 513, 2893
Zaire B., Jouve L., Gastine T., Donati J. F., Morin J., Landin N., Folsom C. P., 2022b, MNRAS, 517, 3392

APPENDIX A: LOG OF OBSERVATIONS

Table A1 summarizes the log of observations collected by the SPIRou spectropolarimeter from 2021 September to 2023 January, and taken as part of CFHT large programmes SLS and SPICE.

Table A1. Log of the SPIRou observations of GM Aur collected from 2021 September to 2023 January. Columns 1 and 2, respectively, give the UT data and the barycentric Julian date derived from the mean observation times of the four subexposures used to derive a polarimetric sequence. Column 3 provides the rotation cycle E obtained using the ephemeris given by equation (1) and column 4 the SNR of the polarization sequences per 2.28 km s^{-1} bin. Average noise levels of Stokes V LSD profiles with respect to the unpolarized continuum level I_c are shown in column 5. Columns 6 and 7 give the EW (with typical uncertainties of 0.01 km s^{-1} , computed as defined in Netzel 2018) and full width at half maximum (FWHM) of veiled Stokes I LSD profiles, respectively. Column 8 displays the RVs obtained from the centroid of a Gaussian fit to the Stokes I LSD profiles and column 9 the error associated with the determination of the centroid position. Similarly, columns 10 and 11 provide RVs and error bars obtained from the LSD profiles built with the CO line mask. Longitudinal magnetic field measurements and standard deviations (see equation 2) are shown in columns 12 and 13, respectively.

Date	Julian Date (+2459 000 d)	E	SNR	$\sigma_{\rm LSD}$ (10^{-4})	EW (km s^{-1})	FWHM (km s^{-1})	RV (km s^{-1})	$\sigma_{\rm RV}$ (km s^{-1})	RV$_{\rm CO}$ (km s^{-1})	$\sigma_{\rm RV_{CO}}$ (km s^{-1})	B_ℓ (G)	σ_{B_ℓ} (G)
(1)	(2)	(3)	(4)	(5)	(6)	(7)	(8)	(9)	(10)	(11)	(12)	(13)
2021 Sept 15	473.06044	2.030	197	1.78	1.06	24.67	15.05	0.10	15.64	0.11	−158	13
2021 Sept 17	475.03513	2.357	201	1.69	1.07	24.41	14.72	0.11	15.24	0.13	−35	13
2021 Sept 19	476.96335	2.676	231	1.42	1.01	24.94	15.30	0.10	15.78	0.12	−108	11
2021 Sept 20	478.01955	2.851	223	1.43	0.94	24.63	15.18	0.11	15.65	0.12	−147	12
2021 Sept 22	480.07583	3.191	238	1.37	1.02	24.90	15.01	0.11	15.57	0.12	−95	11
2021 Sept 23	481.07949	3.358	225	1.64	1.02	24.87	14.61	0.10	15.25	0.12	−30	13
2021 Sept 24	482.07945	3.523	235	1.36	1.05	24.66	14.98	0.09	15.54	0.12	−69	10
2021 Oct 14	502.06869	6.833	224	1.55	0.99	24.58	15.06	0.10	15.74	0.12	−147	12
2021 Oct 16	504.08913	7.167	215	1.81	1.00	24.85	14.87	0.12	15.34	0.13	−111	14
2021 Oct 18	506.07548	7.496	225	1.50	1.01	24.44	14.97	0.10	15.39	0.12	−85	12
2021 Oct 20	508.07626	7.827	224	1.53	0.91	24.43	14.97	0.12	15.71	0.14	−146	14
2021 Oct 21	509.08032	7.993	223	1.57	0.88	24.33	15.20	0.13	16.06	0.14	−134	14
2021 Oct 22	510.07930	8.159	170	1.97	0.84	25.18	14.92	0.14	15.49	0.16	−57	18
2021 Oct 23	511.06749	8.322	232	1.47	1.02	24.82	14.51	0.11	15.35	0.12	−62	12
2021 Oct 25	513.08220	8.656	182	1.66	1.00	25.20	15.04	0.10	15.81	0.12	−119	13
2021 Oct 26	514.04225	8.815	206	1.64	0.96	24.78	15.06	0.11	15.68	0.12	−125	14
2021 Oct 27	515.07220	8.985	226	1.50	1.01	24.39	15.03	0.10	15.61	0.12	−135	12
2021 Oct 28	516.09521	9.155	192	1.66	1.02	25.05	14.85	0.11	15.45	0.13	−99	13
2021 Nov 16	535.09324	12.300	182	1.79	1.01	24.52	14.51	0.11	15.27	0.13	−106	14
2021 Nov 18	537.09010	12.631	170	1.89	1.03	25.09	15.39	0.11	15.97	0.13	−88	15
2021 Nov 19	538.03226	12.787	219	1.55	1.03	24.61	14.79	0.10	15.57	0.12	−105	12
2021 Nov 20	538.97889	12.944	182	1.77	0.99	24.67	14.71	0.10	15.38	0.13	−142	14
2021 Nov 21	539.98340	13.110	232	1.50	1.01	25.38	14.77	0.11	15.17	0.13	−123	12
2021 Nov 22	541.00639	13.279	221	1.43	0.96	24.66	14.35	0.11	15.00	0.12	−121	12
2021 Dec 09	557.97447	16.088	214	1.51	0.91	24.98	14.89	0.11	15.30	0.13	−91	14
2021 Dec 10	558.94112	16.249	196	1.53	0.92	24.67	14.44	0.12	15.30	0.13	−123	14
2021 Dec 11	559.95316	16.416	166	1.86	1.00	24.34	14.95	0.10	15.43	0.13	−111	15
2021 Dec 12	560.95771	16.582	174	1.89	1.00	25.31	15.31	0.10	16.00	0.12	−108	15
2021 Dec 14	563.07065	16.932	200	1.70	0.91	24.05	14.91	0.12	15.78	0.14	−151	15
2021 Dec 15	564.05049	17.094	185	1.71	0.91	25.14	14.65	0.12	15.19	0.14	−79	15
2021 Dec 16	564.98592	17.249	172	1.70	0.94	24.30	14.37	0.11	15.12	0.12	−117	14
2021 Dec 17	566.04362	17.424	182	1.99	1.00	24.22	14.65	0.11	15.26	0.13	−85	16
2021 Dec 18	566.94675	17.574	190	1.79	1.02	25.17	15.27	0.11	15.67	0.14	−96	14
2022 Jan 06	585.93606	20.718	228	1.47	0.94	24.22	14.68	0.12	15.64	0.12	−107	12
2022 Dec 01	915.06659	75.210	224	1.37	1.03	23.86	15.36	0.08	15.67	0.12	−56	10
2022 Dec 02	916.10661	75.382	209	1.45	1.03	24.21	14.48	0.08	15.15	0.13	−118	11

Table A1 – *continued*

Date	Julian Date (+2459 000 d)	E	SNR	$\sigma_{\rm LSD}$ (10^{-4})	EW (km s^{-1})	FWHM (km s^{-1})	RV (km s^{-1})	$\sigma_{\rm RV}$ (km s^{-1})	RV$_{\rm CO}$ (km s^{-1})	$\sigma_{\rm RV_{CO}}$ (km s^{-1})	B_ℓ (G)	σ_{B_ℓ} (G)
(1)	(2)	(3)	(4)	(5)	(6)	(7)	(8)	(9)	(10)	(11)	(12)	(13)
2022 Dec 04	918.07287	75.707	206	1.71	1.07	25.90	15.40	0.11	16.02	0.32	−61	13
2022 Dec 30	944.00911	80.002	214	1.48	1.07	24.96	14.78	0.08	15.42	0.13	−127	11
2022 Dec 31	945.02590	80.170	207	1.50	1.08	25.45	15.41	0.08	15.92	0.14	−56	11
2023 Jan 02	947.01043	80.498	204	1.45	1.06	24.23	15.17	0.09	15.70	0.13	−134	11
2023 Jan 03	947.93475	80.651	203	1.32	1.00	24.45	15.49	0.10	16.01	0.14	−52	10
2023 Jan 05	949.99284	80.992	206	1.42	1.06	24.60	14.55	0.09	15.41	0.12	−127	11
2023 Jan 06	950.87064	81.138	166	1.93	1.07	24.48	14.96	0.10	15.75	0.13	−89	14
2023 Jan 08	952.98862	81.488	173	1.74	1.08	24.44	15.14	0.09	15.69	0.13	−126	13
2023 Jan 09	953.99865	81.655	189	1.41	1.07	25.03	15.63	0.09	16.07	0.12	−52	11
2023 Jan 10	954.95338	81.813	203	1.41	1.07	25.25	14.81	0.10	15.55	0.14	−82	10
2023 Jan 11	955.97002	81.982	209	1.37	1.11	24.83	14.71	0.09	15.47	0.12	−118	10
2023 Jan 12	956.90486	82.137	201	1.42	1.09	24.96	15.30	0.09	15.99	0.13	−68	11
2023 Jan 13	957.94626	82.309	213	1.33	1.06	24.70	14.72	0.10	15.63	0.13	−87	10

APPENDIX B: UNVEILED STOKES LSD PROFILES

We compute unveiled unpolarized (I) and polarized (V) Stokes LSD profiles (from atomic lines) through the relations:

$$I = \frac{\mathcal{W}}{\rm EW} I_{\rm veil} \tag{B1}$$

and

$$V = \frac{\mathcal{W}}{\rm EW} V_{\rm veil}. \tag{B2}$$

Here, veiled unpolarized and polarized LSD profiles are denoted by $I_{\rm veil}$ and $V_{\rm veil}$, respectively. EW is the equivalent width of the pseudo-line profile $I_{\rm veil}$, and $\mathcal{W}$ is a reference equivalent width arbitrarily set to 1.11 km s^{-1} in this paper. Similarly, one can get the SNR of unveiled profiles using the following equations

$${\rm SNR}_I = \frac{\mathcal{W}}{\rm EW} {\rm SNR}_{I\,\rm veil}, \tag{B3}$$

and

$${\rm SNR}_V = \frac{\mathcal{W}}{\rm EW} {\rm SNR}_{V\,\rm veil}. \tag{B4}$$

Figs B1 and B2 illustrate, respectively, time-series unpolarized and polarized LSD signatures of GM Aur before (red lines) and after (black lines) applying the unveiling procedure described above. Comparing both Stokes profiles, it is evident that only minor corrections are needed to mitigate veiling variability at the observation time window. This qualitative finding is consistent with weak veiling variability reported for GM Aur in the literature (McGinnis et al. 2020; López-Valdivia et al. 2021; Bouvier et al. 2023). Line bisectors of the unveiled Stokes I LSD profiles are also displayed in Fig. B1 (dashed black line), following the definition of Gray (1982).

Finally, Fig. B2 also shows null polarization profiles (blue lines). The noise level null signal provides evidence of the optimal extraction of polarized signatures considered in the paper (see Folsom et al. 2016, for a discussion about spurious polarization signals in cool stars).

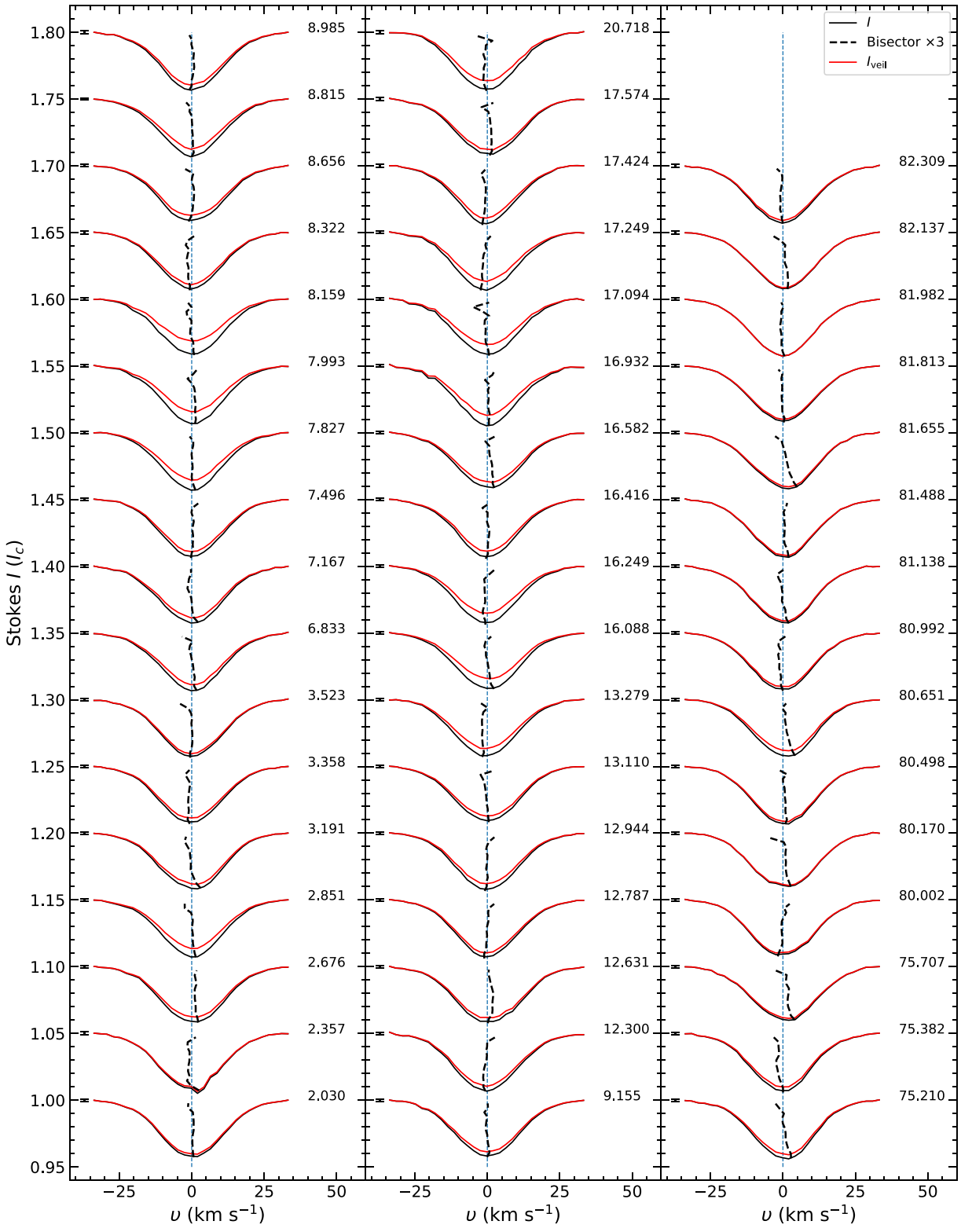

Figure B1. Unveiled (black lines, I) and veiled (red lines, I_{veil}) unpolarized LSD profiles of GM Aur. Line asymmetries are also evidenced when comparing the reference zero velocity (vertical dashed blue line) to the unveiled line bisectors (Gray 1982). Rotational cycles and 1σ error bars are shown next to each profile.

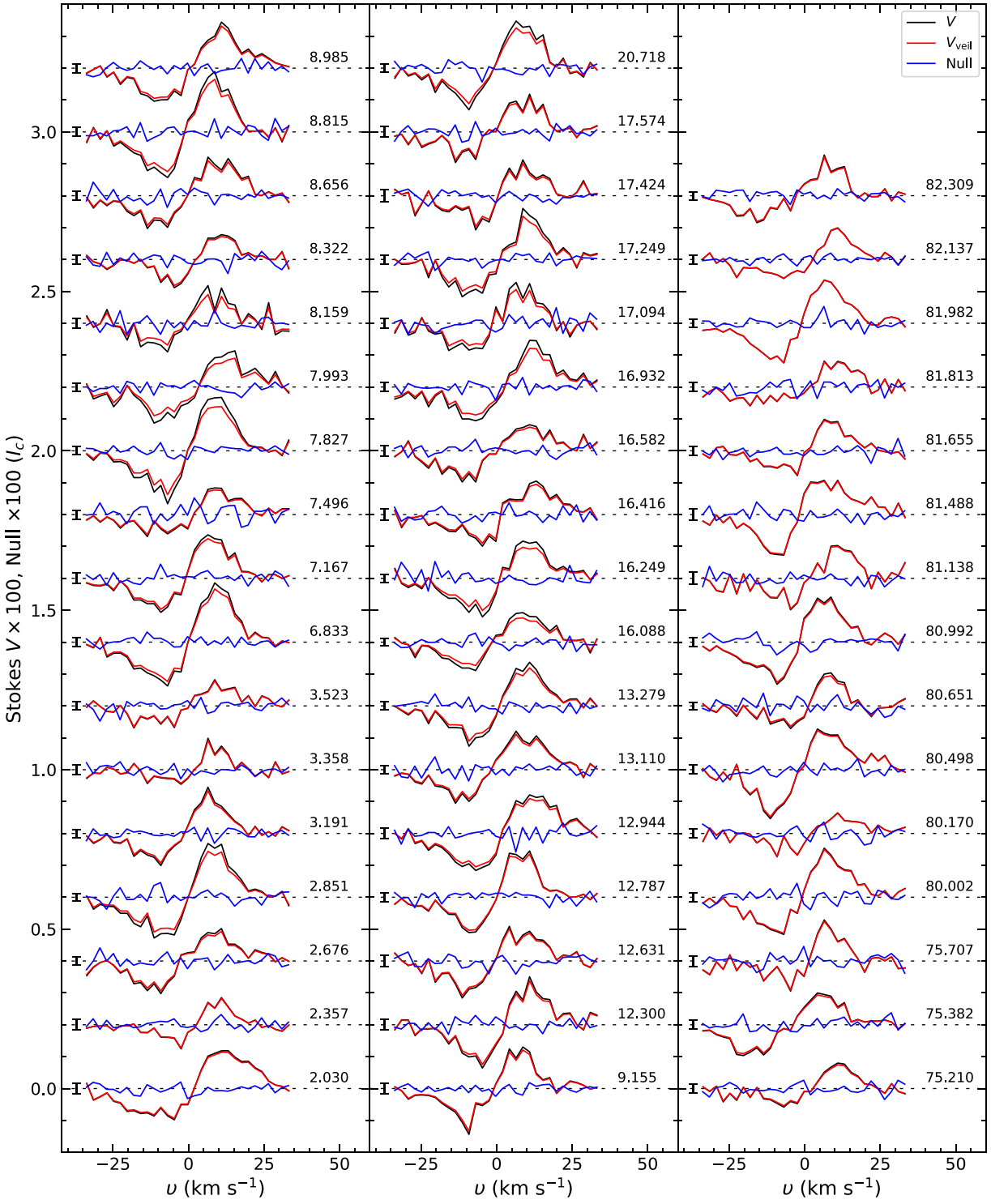

Figure B2. Unveiled (black lines, V) and veiled (red lines, $V_{\rm veil}$) polarized LSD profiles of GM Aur. Control null polarization profiles are shown as blue continuous lines to evidence the lack of spurious polarization signatures in the Stokes V LSD profiles. Rotational cycles and 1σ error bars (scaled following equation B4) are shown next to each profile.

APPENDIX C: ADDITIONAL INFORMATION ON THE RV ANALYSIS

In Section 6, we first considered the activity modelling of the raw RV data from atomic and CO lines. Once the stellar activity was filtered out, we could detect a clear periodic signature in the RVs from CO lines at 8.75 ± 0.02 d. Guided by this periodic signal, we explored a second GP model including the RV wobble induced by a planet in a circular orbit.

C1 Joint fit of the RV data from atomic and CO lines

In Section 6, we discussed the joint modelling of the RV data from atomic and CO lines. Fig. C1 presents the posterior distributions obtained from the MCMC exploration of the 8-parameters allowed to vary in the GP + Planet model. The periodogram of the GP model with a planet is shown in Fig. C2 for the CO line data. We observe a periodic signal at 8.745 d in the activity-filtered RV data (middle panel) and, once the planetary signal is removed (bottom panel), no periodicity remains in the residual data.

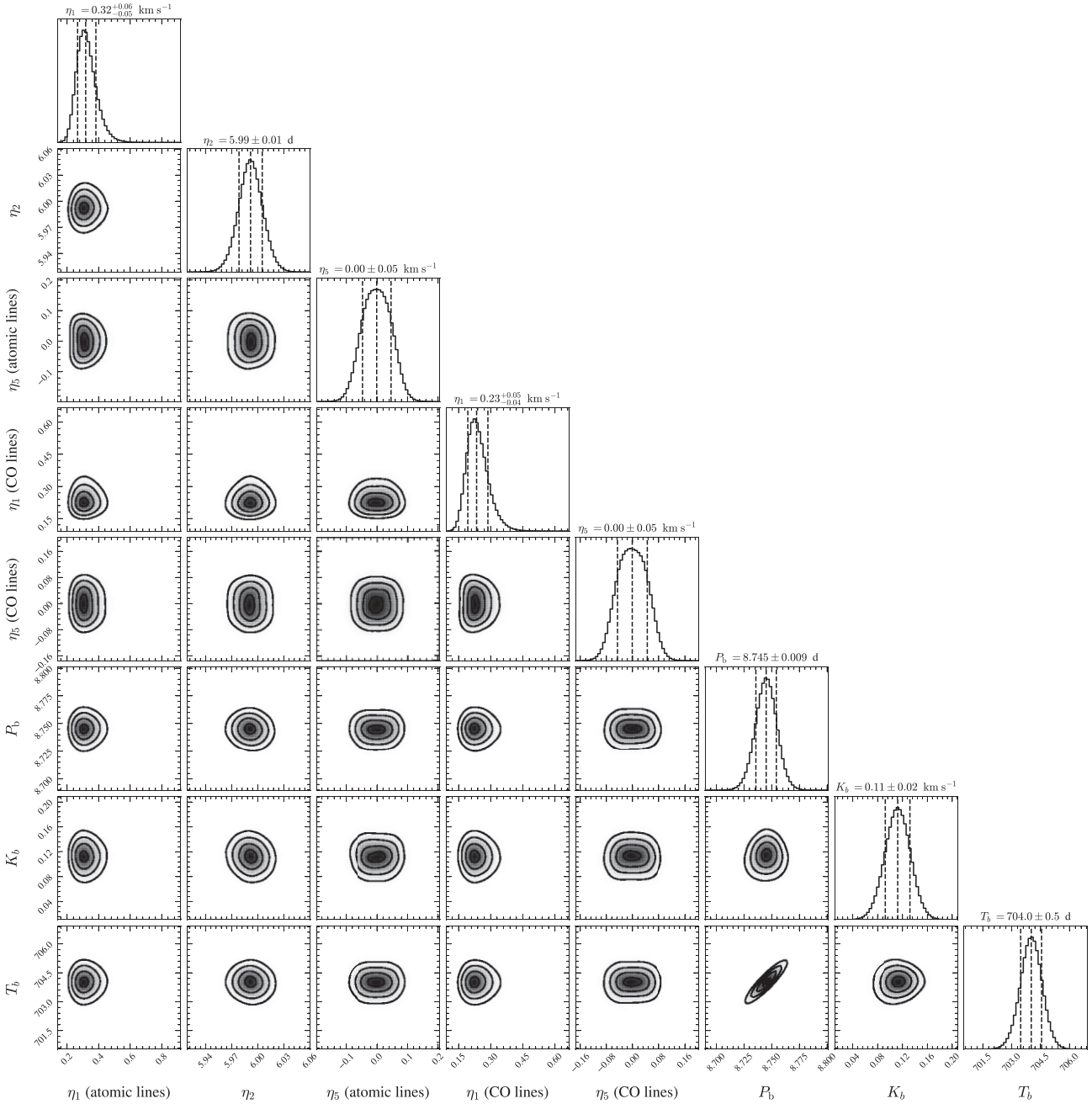

Figure C1. Similar to Fig. 2, but for GP + Planet model of the joint RV data from atomic and CO lines. Semi-amplitude and white noise values are given in km s^{-1}.

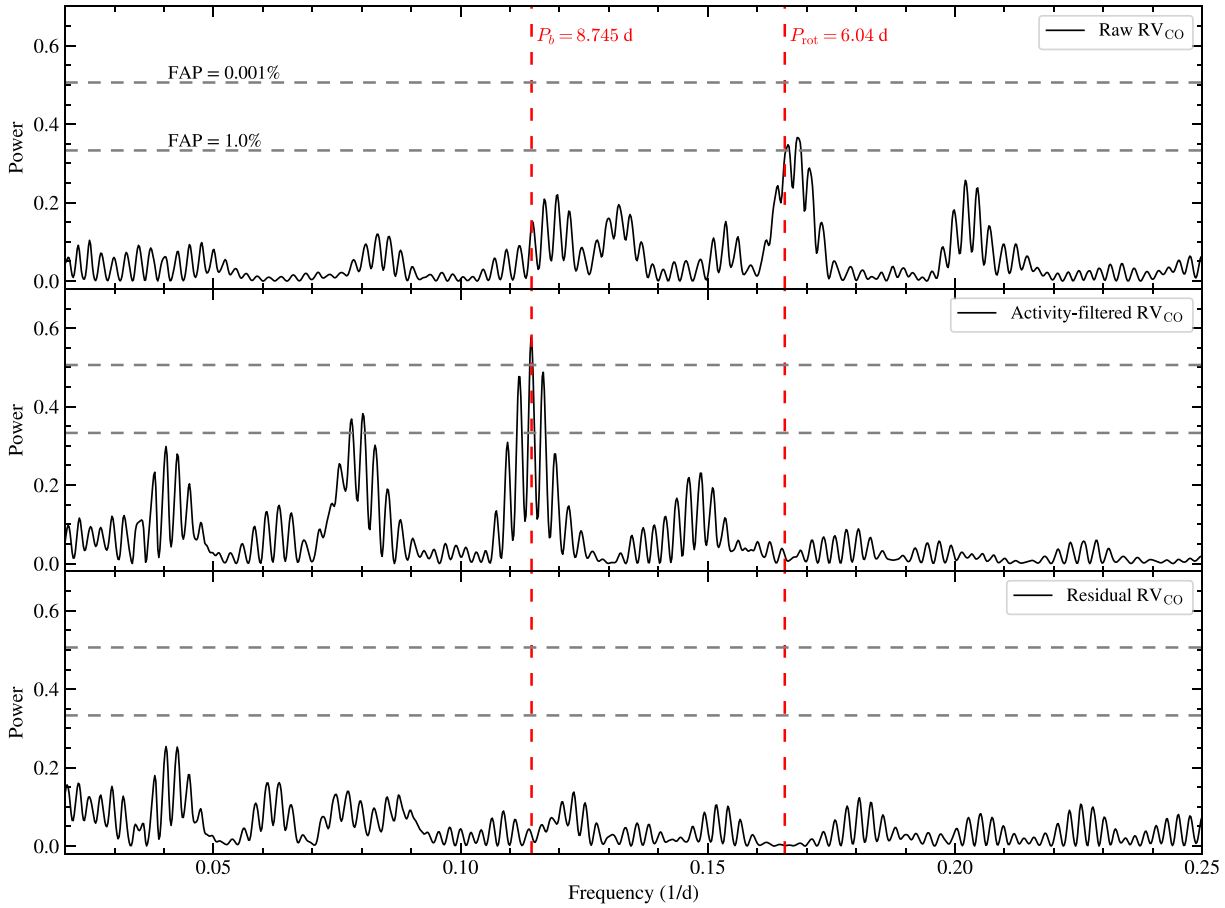

Figure C2. Generalized Lomb–Scargle periodogram computed for the RV data from CO lines. The top panel shows the raw RV data, the middle panel the activity-filtered RV, and the bottom panel the residual RV (i.e. activity- and planetary-filtered RV). The vertical red lines correspond to $P_{\rm rot}$ and P_b, while the horizontal dashed lines illustrate 1 per cent and 0.1 per cent FAP levels. Note that in this figure activity and planet signals are filtered using the solution from the joint (atomic + CO lines) GP model with a planet in a circular orbit.

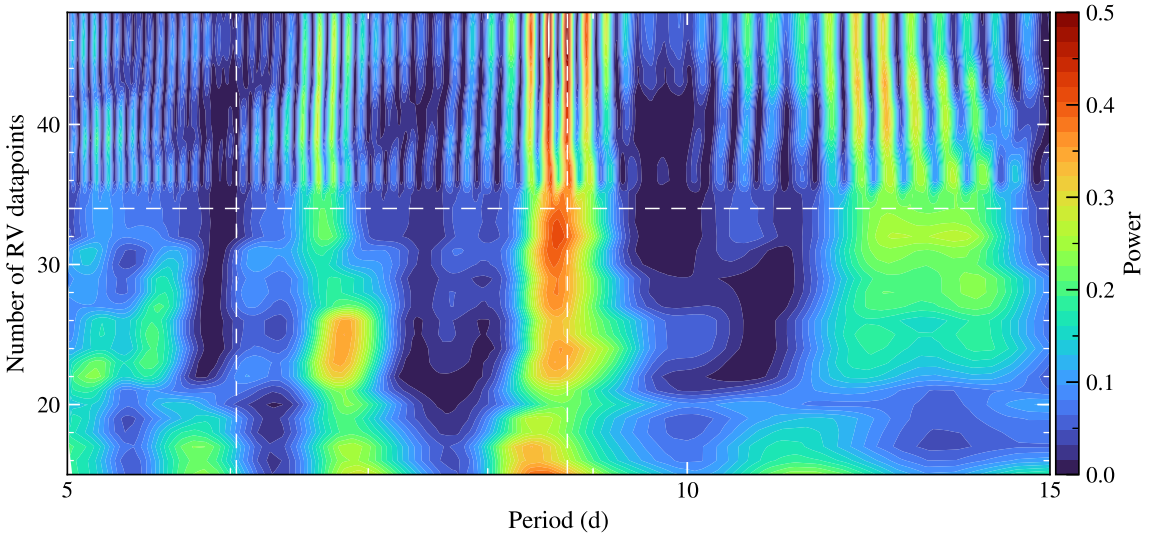

Figure C3. Stacked periodogram of the activity-filtered RV data from CO lines of GM Aur. The vertical dashed lines highlight $P_{\rm rot}$ and P_b, while the horizontal line marks the transition to the last observing season (starting at 2022 December 1). The colour scale depicts the power in the periodogram.

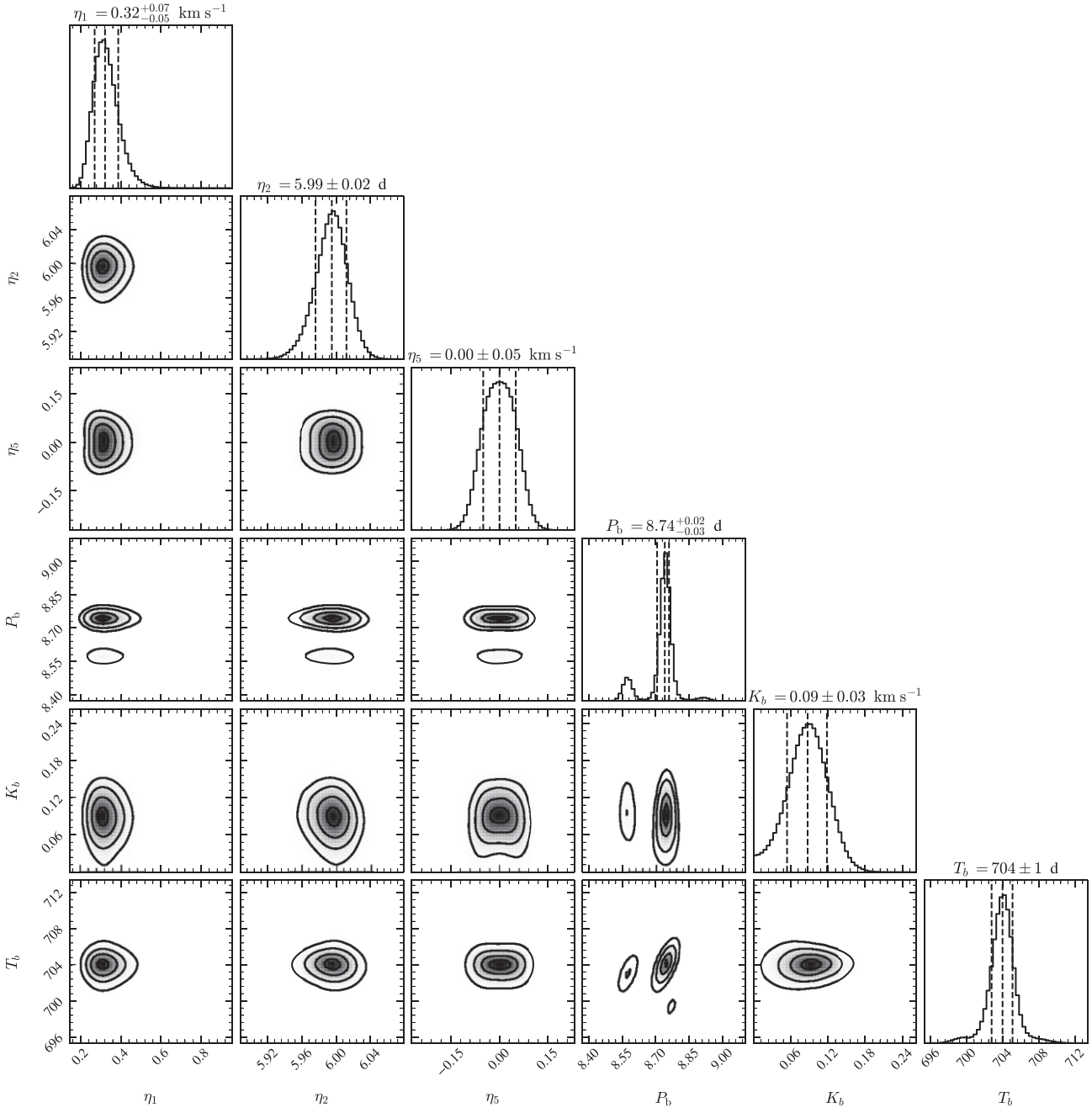

Figure C4. Similar to Fig. C1, but for GP + Planet model of the RV data from atomic lines.

As discussed by Mortier & Collier Cameron (2017), the detection of planet-induced RV signals should increase its significance with the number of observations, contrary to activity signals that are quasi-periodic in nature, as planets induce a coherent signal stable over time. Fig. C3 illustrates how the power of the periodic signal at 8.745 d increases with the number of observations, corroborating the planet detection. We can also note a strong peak at 8.54 d, which corresponds to the 1-yr alias of the true orbital period of 8.745 d.

C2 Independent fit of the RV data from atomic and CO lines

In this section, we illustrate the independent GP regression ran on the RV data from atomic and CO lines. The posterior distributions obtained from the MCMC search are shown in Figs C4 and C5. The planetary solution obtained with the RV data from atomic lines agrees within the error bar with that from CO lines. While the former is detected at a 3σ level, the latter is detected at a 4σ level (see Table 5). Both results are in agreement with the planetary solution found in the joint fit described in the previous section.

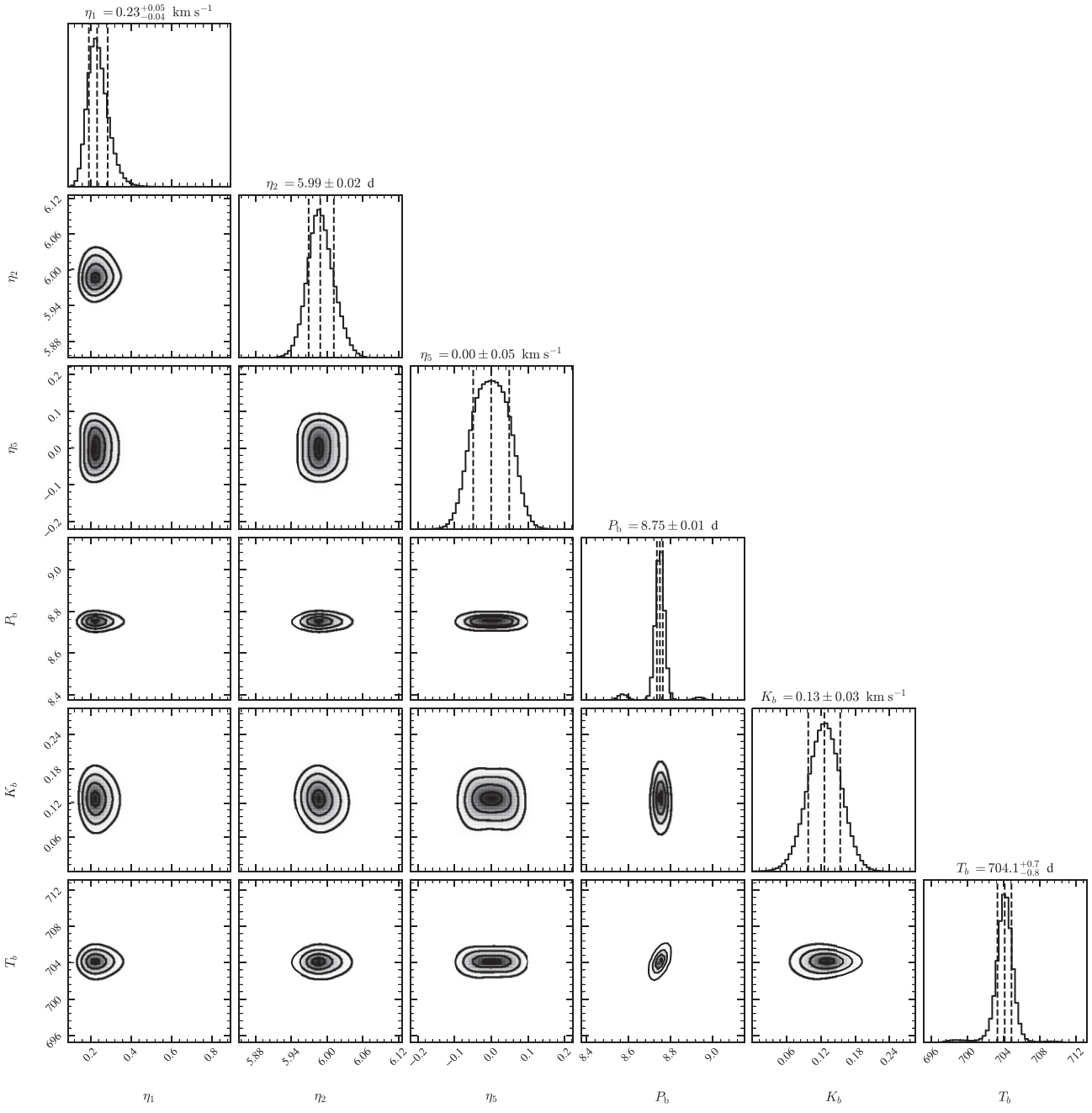

Figure C5. Similar to Fig. C1, but for GP + Planet model of the RV data from CO bandhead lines.

This paper has been typeset from a TEX/LATEX file prepared by the author.